

1 **Optimizing Radar Scan Strategies for Tracking Isolated Deep** 2 **Convection Using Observing System Simulation Experiments**

3 Mariko Oue¹, Stephen M. Saleeby², Peter J. Marinescu^{2,4}, Pavlos Kollias^{1,3}, and
4 Susan C. van den Heever²

5 ¹School of Marine and Atmospheric Sciences, Stony Brook University, Stony Brook, NY, USA

6 ²Department of Atmospheric Science, Colorado State University, Fort Collins, CO, USA

7 ³Environmental and Climate Sciences Department, Brookhaven National Laboratory, Upton, NY, USA

8 ⁴Cooperative Institute for Research in the Atmosphere, Colorado State University, Fort Collins, CO, USA

9 *Correspondence to:* Mariko Oue (mariko.oue@stonybrook.edu)

10 **Abstract.** Optimizing radar observation strategies is one of the most important considerations in pre-field campaign periods.
11 This is especially true for isolated convective clouds that typically evolve faster than the observations captured by
12 operational radar networks. This study investigates uncertainties in radar observations of the evolution of the microphysical
13 and dynamical properties of isolated deep convective clouds developing in clean and polluted environments. It aims to
14 optimize the radar observation strategy for deep convection through the use of high spatiotemporal cloud-resolving model
15 simulations, which resolve the evolution of individual convective cells every 1 minute, coupled with a radar simulator and
16 a cell tracking algorithm. The radar simulation settings are based on the Tracking Aerosol Convection Interactions
17 ExpeRiment (TRACER) / Experiment of Sea Breeze Convection, Aerosols, Precipitation and Environment (ESCAPE) field
18 campaigns held in the Houston, TX area, but are generalizable to other field campaigns focusing on isolated deep
19 convection. Our analysis produces the following four outcomes. First, a 5-7 m s⁻¹ median difference in maximum updrafts
20 of tracked cells is shown between the clean and polluted simulations in the early stages of the cloud lifetimes. This
21 demonstrates the importance of obtaining accurate estimates of vertical velocity from observations if aerosol impacts are to
22 be properly resolved. Second, tracking of individual cells and using vertical cross section scanning every minute captures
23 the evolution of precipitation particle number concentration and size represented by polarimetric observables better than the
24 operational radar observations that update the volume scan every 5 minutes. This approach also improves the multi-Doppler
25 radar updraft retrievals above 5 km above ground level for regions with updraft velocities greater than 10 m s⁻¹. Third, we
26 propose an optimized strategy which is composed of cell tracking by quick (1-2 min) vertical cross section scans from more
27 than one radar in addition to the operational volume scans. We also propose the use of a single range-height indicator updraft
28 retrieval technique for cells close to the radars, where the multi-Doppler radar retrievals are still challenging. Finally,
29 increasing the number of deep convective cells sampled by such observations better represents the median maximum updraft

30 evolution with sample sizes of more than 10 deep cells, which decreases the error associated with sampling the true
31 population to less than 3 m s^{-1} .

32

33 **1 Introduction**

34 The quality and performance of remote sensing measurements, especially radar measurements, can strongly depend on
35 the siting of instruments relative to their targets and the associated sampling strategies (e.g., Bousquet et al., 2008; Potvin
36 et al., 2012b; Oue et al., 2019). This is especially true for convective storm systems that evolve rapidly over a range of
37 spatial and temporal scales. The limitations associated with observation strategies influence microphysical, dynamical, and
38 convective-core property retrievals, resulting in a misinterpretation of the observational data and can limit our understanding
39 of storm processes. Some of these limitations can be addressed using Model and field Experiment data fusion (ModEx)
40 concepts such as the optimization of experimental design using models and forward simulators. Using the ModEx
41 framework, one can appropriately determine optimal radar deployments and scan strategies, as well as quantitatively
42 understand the observational uncertainties arising from these strategies before field campaigns begin. As such, the goal of
43 this study is to suggest optimal radar deployments and scan strategies for radar field campaigns targeting isolated convective
44 clouds.

45 The limitations in the radar observations that are mostly attributed to sampling strategy strongly impact the radar-based
46 retrievals of geophysical quantities and cloud properties (e.g., Clark et al., 1980; Given and Ray, 1994; Collis et al., 2010).
47 These sampling strategy choices include scanning time (scan rate) for a volume scan, spatial resolution (azimuth/elevation
48 spacings and range-gate spacing), elevation angles for plan position indicator (PPI) volume scans, distance to the target
49 phenomena from the radars (this is also related to the spatial resolution), systematic variability (i.e., noisiness) in the
50 observables, and data smoothing and interpolation for gridding the data. In particular, the sampling strategy can significantly
51 impact the uncertainties in vertical velocity retrievals (e.g., Oue et al., 2019), which are important for the analysis of cloud
52 microphysics and dynamics. In addition, the retrievals include uncertainties attributed to assumptions in their algorithms;
53 for instance, some multi-Doppler radar-based vertical velocity retrievals must make assumptions for the particle fall speed
54 and mass continuity (e.g., North et al., 2017).

55 In operational radar networks (e.g., the Next Generation Weather Radar (NEXRAD) network), each radar performs
56 volume scans consisting of plan position indicator (PPI) scans with multiple elevation angles to prioritize collecting data
57 for large areas. The volume scan strategy (known as volume coverage pattern, VCP) takes approximately 5 minutes to
58 collect the 3D atmospheric data. While this operational scanning strategy is very valuable for performing surveillance and
59 collecting a large number of cloud samples, it may not accurately capture fine-scale, rapidly-developing cloud phenomena.
60 To increase our understanding of the links between convective cloud kinematic and microphysical processes, field
61 campaigns have recently started to focus on collecting observations at higher temporal and spatial resolutions to understand
62 fine-scale characteristics and phenomena including isolated convection, shallow cumulus clouds, plumes embedded in
63 mesoscale systems, convective updrafts and downdrafts (e.g., Verification of the Origins of Rotation in Tornadoes

64 Experiment 2 (VORTEX2), Wurman et al., 2012; Midlatitude Continental Convective Clouds Experiment (MC3E), Jensen
65 et al., 2016; CSU Convective Cloud Updraft and Downdraft Experiment (C³LOUD-Ex), van den Heever et al., 2021;
66 Marinescu et al., 2020), and high-latitude precipitation (e.g., Light Precipitation Evaluation Experiment (LPVEx), L’Ecuyer,
67 et al., 2010). Furthermore, in some of these field campaigns, physically tracking individual convective phenomena using
68 cutting-edge mechanically scanning radar systems was employed to prioritize high spatiotemporal sampling (e.g., The
69 Dynamical and Microphysical Evolution of Convective Storms (DYMECS), Stain et al., 2015; Iowa Flood Studies
70 (IFloodS), Mishra et al., 2016). The high-spatiotemporal resolution observations can also be achieved by complementing
71 the operational radar networks with adapting scan strategies of the regional research radars that have been installed in local
72 areas. (e.g., Distributed Collaborative Adaptive Sensing (DCAS), McLaughlin et al., 2005; Multi-sensor Agile Adaptive
73 Sampling (MAAS), Kollias et al., 2020).

74 In recent years, as phased array weather radars (PARs) have become more commonly used for severe weather
75 observations, the sophisticated tracking of atmospheric phenomena has become feasible (e.g., Kollias et al., 2022). The
76 PARs have a significant advantage of sampling rapidly evolving atmospheric phenomena at high-temporal resolutions (e.g.,
77 Billam and Harvey, 1987; Heinselman and Torres, 2011; Mahre et al., 2018; Griffin et al., 2019; Adachi and Mashiko, 2020;
78 Moroda et al., 2021), thus allowing for sampling of the entire cloud volume and cloud lifecycle. The tracking observations
79 obtained by these rapid scanning radar or PAR systems are, however, more sensitive than previous approaches to scan
80 strategies such as sampling time, azimuth/elevation spacings, and deployments (locations and the number of radars), all of
81 which should be appropriately optimized depending on the spatial scale and evolution speed of the target phenomena
82 (Kollias et al., 2020).

83 Several radar field campaigns aim at enhancing our understanding of the links between convective cloud kinematic and
84 microphysical processes and life cycles (e.g., Tracking Aerosol Convection Interactions Experiment (TRACER), Jensen et
85 al., 2019; Experiment of Sea Breeze Convection, Aerosols, Precipitation and Environment (ESCAPE); Jensen et al., 2022;
86 Atmospheric Radiation Measurements (ARM) Mobile Facility 3 (AMF3) Southeast US deployment, Kang et al., 2021). All
87 of these experiments have deployed or plan to deploy multiple mobile weather radars, cloud radars, rapid-scan radars, and
88 phased array radars. In particular, TRACER and ESCAPE campaigns focus on observing isolated deep convective storms
89 with different aerosol environments. Optimizing the radar deployments and scan strategies while taking into account
90 campaign costs, deployment limitations, and sampling limitations (i.e., range, scan rate) is a large but critical challenge.
91 Observing system simulation experiment (OSSE) is a powerful tool to investigate the impact of the limitations on the
92 observation analyses (Oue et al., 2020), and using high-spatiotemporal data is needed to reliably simulate the observations
93 accounting for the limitations. While the focus of this study has been on the TRACER/ESCAPE field campaigns, the results
94 are generalizable to other future campaigns focused on isolated deep convection. In this paper we make use of OSSEs
95 focused on deep convection to specifically investigate the impacts of radar scan strategies on the cell tracking performance,
96 microphysical evolution, and dynamical retrievals of convective storms. Specifically, the impacts of varying the scan
97 elevation angles, the period for a volume scan, and the locations of the radars are assessed.

99 **2 Method**

100 Our OSSE approach is comprised of three parts: (1) the Regional Atmospheric Modeling System (RAMS; Cotton et al.,
101 2003; Saleeby and van den Heever, 2013); (2) the Cloud-resolving Radar Simulator (CR-SIM; Out et al., 2020); and (3) the
102 Tracking and Object-Based Analysis of Clouds (*tobac*; Heikenfeld et al., 2019; Sokolowsky et al., 2022). Figures 1a-1c
103 show example snapshots from parts (1) and (2), and Figure 1d shows the tracking result from the part (3). RAMS model
104 output from the Aerosol-Cloud-Precipitation-Climate (ACPC) model intercomparison project (MIP) (van den Heever et al.,
105 2018; Marinescu et al., 2021), which focuses on the development and occurrence of isolated convective cells in the region
106 around Houston, TX, on June 19-20, 2013 (Fig. 1a), forms the basis of this study. The convective development was initiated
107 both along the inland propagation of the sea breeze, and later in association with convective cold pools produced by the
108 earlier convection in the simulation. In this study we focus on the time period from 20-24 UTC (15-19 local time) during
109 which deep convective clouds developed, the dynamical processes of which have been extensively analyzed (Marinescu et
110 al., 2021). One-minute simulated deep convective fields are used as an input to CR-SIM to represent and evaluate the radar
111 observable fields (Fig. 1b). The CR-SIM radar observables are subsequently used to track convective cells using *tobac*.

112 **2.1 CR-SIM**

113 CR-SIM is a sophisticated radar forward operator developed to bridge the gap between high-resolution cloud model
114 output and radar observations (Oue et al., 2020). CR-SIM can be applied to the 3D model output produced by a variety of
115 cloud-resolving models and large-eddy simulation models, including RAMS, the Weather Research and Forecasting (WRF,
116 Powers et al., 2017) model, the System for Atmospheric Modeling (SAM, Khairoutdinov and Randall, 2003), Cloud Model
117 1 (CM1, Bryan and Fritsch, 2002), and the Icosahedral Nonhydrostatic model (ICON, Zängl et al., 2015). It emulates the
118 interaction between transmitted polarized radar waves and rotationally symmetric hydrometeors and can simulate the power
119 (equivalent radar reflectivity factor), phase (Doppler velocity), and polarimetric (specific differential phase, differential
120 reflectivity, depolarization) variables with either a fixed elevation angle or varying elevation angles with respect to a
121 specified radar location. CR-SIM outputs these variables on the same grid as the input model grid. The radar simulator has
122 been shown to be especially effective in OSSEs to investigate the uncertainties in observational data (Oue et al., 2019).

123 **2.2 *tobac***

124 *tobac* is a python-based software platform specifically developed for tracking atmospheric features, such as isolated
125 convective cells, in both model and observational datasets. *tobac* has been developed using a modular code structure with
126 data input, feature detection and segmentation, and trajectory linking steps. It uses a watershed algorithm to detect and track
127 individual convective cells, and it has been extensively tested on the ACPC simulations (e.g., Heikenfeld et al., 2019;

128 Marinescu et al., 2021). For this study, *tobac* Version 1.2 is applied to CR-SIM vertically integrated liquid (VIL; Fig. 1c),
129 which represents the total hydrometeor condensate within each vertical column and is similar to the approach used by Hu
130 et al. (2019). The CR-SIM radar reflectivity is converted into VIL using the following equation:

$$131 \quad VIL = \sum_{i=0}^{i=imax} 3.44 * 10^{-6} [(Z_i + Z_{i+1})/2]^{4/7} (h_{i+1} - h_i) \quad [kg \ m^{-2}] \quad (1)$$

132 where Z is radar reflectivity factor ($mm^6 \ m^{-3}$), h is height (m), i is the vertical index, and $imax$ is the index at the grid
133 domain top. We calculate VIL using the CR-SIM-simulated total reflectivity greater than or equal to 0 dBZ at all vertical
134 levels and, thus, ensure that we consider all cloudy grid boxes in the tracking analysis. Although this variable is named
135 ‘liquid,’ we use the total reflectivity from all simulated hydrometeor species to emulate real observations, including cloud
136 droplets, drizzle, rain, cloud ice, snow, aggregates, graupel, and hail. Since “VIL” is a widely-used name, we refer to VIL
137 as this parameter. When considering that clouds may have lower reflectivity (< 0 dBZ) and the radar minimum detectable
138 reflectivity increases with distance from the radar, the reflectivity threshold of 0 dBZ for the VIL calculation is a reasonable
139 value to use in detecting cells in the entire domain regardless of the distance. We also performed the cell tracking using 10
140 and 40 dBZ thresholds at the height of 2 km above ground level (AGL) to compare the performance of the use of VIL and
141 single-level reflectivity thresholds.

142 **2.3 RAMS**

143 RAMS is a cloud-resolving model that includes sophisticated microphysical-dynamical feedbacks, as well as aerosol-
144 cloud interactions (Saleeby and van den Heever, 2013). RAMS, along with several other cloud resolving models from
145 around the world participated in the ACPC MIP, focuses on the effects of changing the concentrations of cloud condensation
146 nuclei (CCN) on deep convective clouds (van den Heever et al., 2018). Case study simulations of a period of scattered
147 convective clouds near Houston, Texas were completed with relatively low and high concentrations of CCN that were based
148 on observations from the Houston area (see Figure 2 from Marinescu et al., 2021). The low-CCN simulation is initialized
149 with 500 cm^{-3} of CCN in the boundary layer (named CLN in this study), while the high-CCN simulation is initialized with
150 4000 cm^{-3} of CCN in the boundary layer (named POL in this study). The vertical aerosol profiles of both the CLN and POL
151 studies decrease linearly from the top of the boundary layer to 150 cm^{-3} at ~ 5 km AGL (the free troposphere), above which
152 they remain constant. RAMS allows for the advection, nucleation, wet and dry deposition, and regeneration of aerosol
153 particles via hydrometeor evaporation and sublimation. These simulations have been performed using a horizontal grid
154 resolution of 500 m and RAMS’ two-moment bin-emulating bulk-microphysics scheme, which predicts the mass and
155 number of eight hydrometeor types. The model data are output at a frequency of 1-minute. Additional details about the
156 RAMS model parameterizations and experimental setup used for these simulations can be found in Table 1 of Marinescu et
157 al. (2021).

158 **2.4 Observation simulation processes**

159 In this study, the cell tracking is applied to the CR-SIM-simulated radar observation field (VIL) to detect and track
160 individual convective storm cells. Using the tracking results for all cells, we investigate the performance of the cell tracking
161 using VIL, the impact of the scan strategy on the VIL estimates (Sect. 3.1), and the statistical impact of aerosols on the cell
162 dynamical evolution (Sect. 3.3). One of the tracked, isolated, deep convective cells with a single precipitation core is chosen
163 to investigate the following: 1) the impacts of the scan strategy on the examination of polarimetric observables and related
164 microphysical studies (Sect. 3.2); and 2) the influences of different sets of the scan strategies on the multi-Doppler vertical
165 velocity retrievals (Sect. 3.3). The chosen cell is representative of isolated deep convective cells from the CLN simulation
166 (discussed in Sect. 3.2).

167 **2.4.1. Tracking convective cells**

168 The *tobac* cell tracking is coupled with CR-SIM radar observables obtained using the RAMS model output in the
169 following manner:

- 170 1) The RAMS model output from the ACPC MIP for an isolated convective case over the Houston area (Fig. 1a) is
171 used as input to CR-SIM.
- 172 2) The radar observable fields (Fig. 1b) are simulated using CR-SIM and output on the same grid as the input model
173 grid.
- 174 3) The CR-SIM simulated radar reflectivity is converted into VIL if the reflectivity exceeds 0 dBZ at all levels
175 (Fig.1c).
- 176 4) *tobac* is applied to the VIL field to track the convective cells (Fig. 1d). We used the VIL thresholds of 0, 0.1, 1.0,
177 and 5.0 kg m⁻² to identify/track individual cells, including those embedded in larger precipitation areas.
- 178 5) Steps 1-4 above are applied to the CLN and POL RAMS simulations to investigate the impact of aerosols on the
179 cell dynamical evolutions in the entire simulation domain.

180 **2.4.2. Emulating radar scan strategies**

181 We emulate the radar scan strategies to account for observational limitations including scanning time for a volume scan,
182 azimuth/elevation angle spacings, range-gate spacing, elevation angles for PPI volume scans, distance to the target
183 phenomena from the radars, and smoothness and interpolation for gridding process. This study tests the sensitivity of updraft
184 retrievals to four of these scanning strategy choices: i) scanning time, ii) elevation angle spacing, iii) distance to the targeted
185 convective cell, and iv) the number of radars used for the updraft retrievals. This section explains how the scan strategies
186 are emulated using CR-SIM.

187 The various radar scan strategies emulated in this study are listed in Table 1. We first emulate cell tracking using sector
188 range-height indicator (RHI) scans, each of which is composed of full elevation angles from 0.5° to 89.5° with a 1° increment

189 in an azimuth sector and takes approximately 1 minute (1-min RHI in Table 1). The 1-min RHI scan uses a snapshot of data
190 to complete a full elevation scan for a sector. For mechanically scanning radars, 1-min RHI may not be feasible due to
191 mechanical limitations (e.g., overhead time needed when changing the antenna sweep direction), and those radars may need
192 more time to complete the sector scans (as discussed later in this section).

193 The second emulation of cell tracking is also a full elevation scan for an azimuth sector similar to 1-min RHI but takes
194 2 minutes using two continuous snapshots (2-min SEC). To construct the cells observed by the sector scan that takes 2 min,
195 we use two consecutive model snapshots; the first snapshot at the earlier time is used to simulate the scan for angles from
196 0.5° to 44.5° over the elevation, and the other is used to simulate the scan for the angles from 45.5° to 89.5° over the
197 elevation (we intend this simulation to represent a 2-min “RHI” in which each of the two snapshots should be used for a
198 half of the azimuth sector for full elevation angles, however, for technical and computational reasons, we separate the
199 elevation angles into the two snapshots). This 2-min SEC simulation is performed every 2 min.

200 The tracking cell by 1-min RHI and 2-min SEC is guided by *tobac* using the VIL estimate from the model full grid every
201 1 minute. The azimuth sectors for 1-min RHI and 2-min SEC are decided so that each azimuth sector covers the 10-km
202 width centered around the individual cells defined by *tobac*. Therefore, the number of RHI sweeps for each cell varies as a
203 function of the distance between the radar and the target cell. The radar configuration for the RHI simulation is assumed to
204 be a general scanning radar such as the ARM precipitation radars. The angle range for an azimuth sector at the radar range
205 of 40 km is approximately 14° . With the radar beam width of 1° , the total beam for the sector scan is 90 (over elevation) x
206 14 (over azimuth) = 1260 beams. Assuming that each beam uses ~96 radar pulse samples, the sector scan includes 120960
207 pulses in total. If the radar operates with 1.5 KHz pulse repetition frequency (PRF) (typical value for C-band radars), then
208 the sector scan takes 80 sec; and if the radar operates with 2.5 kHz PRF (typical value for X-band radars), then the scan
209 takes 48 sec. These numbers (scans within 1-2 min) are easy to get for phased-array radar observations. For a reflector
210 (mechanical scan) radar that needs 33% overhead time due to acceleration and deceleration of the antenna, these scan times
211 become 106 sec and 64 sec respectively.

212 The third strategy we investigate is the 5-min VCP. This strategy follows the standard NEXRAD VCP precipitation
213 mode (VCP 12, https://www.weather.gov/jetstream/vcp_max) and is composed of 14 PPI scans. Since our model output is
214 every minute, for the 5-min VCP simulation, a volume scan is composed of 5 snapshots from the 1-min model outputs. A
215 single snapshot is used to create two or three PPI sweeps (two or three elevation angles).

216 Finally, for the fourth strategy, we evaluate an “ideal” simulation where a volume scan with full elevation and azimuth
217 scans with a 1.0° increment over both elevation and azimuth is performed within 1-min (referred to as “Full” in Table 1).
218 This approach will be feasible when a network of rapid scan or electronically scanning radars is available. Although such
219 observations are not realistic, they can serve as an upper boundary in terms of observational capabilities and will be used
220 for an evaluation of VIL from 5-min VCP in Section 3.1.

221 We use an S-band frequency for the 5-min VCP simulation (emulating NEXRAD radars) and a C-band frequency for
222 1-min RHI, 2-min SEC, and Full simulations (assuming the C-band Scanning ARM Precipitation Radar (C-SAPR), or any

223 equivalent performance radar). Since we use unattenuated radar observables in this study, the impacts of the radar frequency
224 on the simulation results should not be significant.

225

226 **2.4.3. Multi Doppler radar wind retrieval**

227 For the investigation of the impacts of scan and deployment strategies on multi-Doppler vertical velocity retrievals, this
228 study employs a three dimensional variational (3DVAR) multi-Doppler radar wind retrieval technique developed by North
229 et al. (2017). While this investigation focuses on uncertainties caused by scan and deployment strategies, it does not account
230 for other sources of errors such as attenuation, nor the particle fall speed assumed in the 3DVAR wind retrieval technique.
231 We use unattenuated radar reflectivity and reflectivity-weighted fall speed calculated by CR-SIM in all present wind
232 retrieval simulations. The details of the 3DVAR retrieval settings are presented in Oue et al. (2019). As described in Oue et
233 al. (2019), the 3DVAR wind retrieval technique is applied to the gridded radar observable fields. The radar observables that
234 are resampled following the radar scan strategies in the previous sections are then re-gridded into a Cartesian coordinate of
235 250 km x 250 km x 14 km domain with 0.25-km horizontal and vertical spacings using Barnes distance-dependent
236 weightings (Barnes, 1964).

237

238 **3. Results**

239

240 **3.1 Evaluation of the tracking parameter**

241 This study employs VIL as a tracking parameter and, as such, is similar to Hu et al. (2019). The use of VIL allows us
242 to consider hydrometeor condensate at all levels, whereas previous convective cell tracking studies have employed
243 reflectivity criteria at a given height (e.g., Steiner et al., 1995; Shusse et al., 2006; Oue et al., 2014). Tracking based on
244 reflectivity at a single height may well define individual cells especially for embedded cells in stratiform regions, however,
245 it can miss some of the early stages of convective cell development that initiate at different (typical lower) heights. In this
246 section, we evaluate VIL as a tracking parameter for the simulations used in this study. Figure 2a shows a comparison of
247 the durations of *tobac* detected and tracked cells in the CLN simulation as a function of the use of VIL, as well as 10 and
248 40 dBZ thresholds at 2 km altitude. The time bin size used for Fig. 2 is 5 min. The VIL-based tracking has the largest total
249 number of cells detected since the VIL better captures the presence of hydrometeor condensate throughout the vertical
250 columns and is not dependent on the presence of condensate at a specific level. All of the frequency distributions, perhaps
251 unsurprisingly, peak at shorter durations for both CLN and POL cases. The VIL-based and 10-dBZ-based tracking are more
252 comparable, although the VIL-based tracking has higher frequencies at even longer durations (> 90 min) compared to the
253 10-dBZ-based tracking. The 40-dBZ-based tracking generally has lower frequencies at all duration time bins compared to
254 the 10-dBZ- and VIL-based tracking, but it is more similar to the 10-dBZ-based tracking in the 25–40 minute time bins.
255 The frequency distributions of tracked cell lifetimes suggest that VIL can better capture longer life cycles of individual cells,

256 including their initial development and decay stages, due to its ability to include information about hydrometeors in the
257 entire column.

258 The POL simulation (dashed line in Figure 2a) shows a similar tracked cell lifetime distribution to the CLN case.
259 However, there are some notable differences. The POL case has fewer cells detected (~15% fewer for VIL), which is
260 consistent with Marinescu et al. (2021), who also found fewer deep convective updrafts in the POL case using different
261 analyses (their Figure 7). When considering the relative frequency distribution (not shown), the POL case also has a
262 distribution shift towards relatively fewer long-lived cells (lifetimes > 20 mins) and more frequent short-lived cells (lifetimes
263 < 20 mins), as compared to the CLN case. The relatively fewer long-lived cells in the POL case are associated with deep
264 convection. There could be several reasons for the difference in cell lifetimes related to microphysical-dynamical feedback
265 processes, such as those associated with cold pools (e.g., Grant and van den Heever, 2015). These differences between CLN
266 and POL are being examined in a separate manuscript. Hereafter, we use the CLN case to examine the effects of scan
267 strategy on the radar polarimetric observables and vertical velocity retrievals. The difference in the number of cells detected
268 is consistent between the three tracking criteria. However, the difference in lifetime is clearest in VIL, being slightly evident
269 in 10-dBZ-based, but unclear in 40-dBZ-based. This suggests that the VIL-based tracking is more sensitive to the difference
270 in cell lifetimes between the CLN and POL simulations, and therefore, may be suitable for tracking isolated convective cells
271 throughout their lifetimes and quantifying cell-lifetime statistics. This may work for the cases where isolated cells dominate
272 in the domain with less stratiform or mesoscale precipitation areas. In such cases, the features identified by *tobac* in the VIL
273 field well represent individual clouds (i.e., a single detected feature rarely includes more than one cells).

274 Since VIL integrates reflectivity from the surface to the observed echo top, it better captures hydrometeor condensate
275 in the entire vertical column. This is especially effective for conventional VCP scanning that may miss cells at a specific
276 height if they are very close to the radar or far from the radar. On the other hand, the conventional VCPs that do not include
277 higher elevation angles or that have sparse elevation scans, therefore, tend to produce an underestimation of VIL. Moreover,
278 averaging inhomogeneities within large range-bin volumes, which occur at distances far from the radar, can also cause
279 uncertainties when using VIL. To assess these uncertainties, we investigate the VIL as a function of distance from the radar.

280 Figure 3 compares contoured frequency by distance distributions of VIL from the 5-min VCP and Full scan (from 0°
281 to 90° over elevation) strategies. Although we use the horizontal distance from the radar instead of altitude in constructing
282 our contoured frequency by altitude diagram, we use the term 'CFAD' to refer to this kind of distribution diagram in this
283 study. Overall, both scans produce small differences in the frequency of less than 0.05 in the CFADs, except within the 30
284 km range from the radar. For 5-min VCP, there is a shift to higher frequencies of smaller VIL values (red color at distance
285 < 30 km and < -12 dB in Fig. 3b). At distances within 30 km of the radar, both radars have sufficient sensitivity (< -9 dBZ).
286 This underestimation is, therefore, likely due to the fact that 5-min VCP does not observe the upper parts of the clouds. The
287 smaller differences that occur at distances > 90 km, which are shown in both scan strategies, are likely due to the minimum
288 detectable reflectivity, which increases with distance from the radar. It can be concluded that even the NEXRAD VCP

289 captures the VIL well except for distances less than 30 km from the radar and is, thus, very valuable for the surveillance of
290 convective cells and is also useful to detect and subsequently track targeted cells, as well as guide the cell tracking using
291 RHI measurements.

292

293 **3.2 Evolution of polarimetric variables associated with microphysics**

294 Polarimetric observables (e.g., differential reflectivity Z_{DR} and differential propagation phase K_{DP}) have frequently been
295 used by past studies as an indicator of microphysical and updraft evolution (e.g., Kumjian and Ryzhkov, 2008; Kumjian et
296 al., 2014; Snyder et al., 2013). The NEXRAD polarimetric measurements are very important for capturing the precipitation
297 microphysical properties. However, its poor spatiotemporal sampling (i.e., limited PPI elevation angles, time for volume
298 scan) provides only a limited view in convective storms (Fridlind et al., 2019). Here, we assess the impact of the NEXRAD
299 spatiotemporal sampling by simulating the polarimetric observables from the 1-minute RHI tracking (1-min RHI in Table
300 1) and the 5-minute conventional PPI volume scan (5-min VCP in Table 1). We randomly select 12 cells from the 453 deep
301 convective cells tracked in the CLN simulation. These cells all have maximum radar reflectivity exceeding 45 dBZ and 20-
302 dBZ echo top heights greater than 8 km AGL during their lifetime. We then examine the evolution of microphysical and
303 dynamical characteristics such as number concentration and mean diameter for each simulated hydrometeor species, as well
304 as the vertical velocity. Nine of the cells have 40-dBZ mean echo top heights that exceed the freezing level (approximately
305 5 km AGL) and attain 8 km altitude, which signify stronger convection. These 9 cells show similar evolution of K_{DP} , Z_{DR} ,
306 and maximum updrafts, all of which have magnitudes greater than 20 m s^{-1} in the middle of their lifetimes. Three of the
307 twelve cells do not have 40-dBZ echo top heights extending above the freezing level. From the 9 vigorous, deep convective
308 cells, one representative cell is chosen for a detailed OSSE analysis based on its isolated nature and development near the
309 NEXRAD radar and other radar locations, used for TRACER and ESCAPE. While we focus on one cell only, the results
310 can be extended to the other deep isolated cells. Figure 4 shows the evolution of the mass-weighted mean diameter (D_m)
311 and number density for the rain and hail species for the chosen cell. Large rain D_m ($> 1.5 \text{ mm}$) is evident near the freezing
312 level (dashed line) during the later stage of the cell lifetime as the echo top height descends (after 21:50 UTC in Fig. 4c).
313 Around this time, the largest D_m for hail is also apparent (Fig. 4d). This indicates that the large hail melts as it falls through
314 the freezing level, thereby producing large raindrops. The hail number concentration (Fig. 4f) is also strongly correlated
315 with updraft magnitude (Fig. 4b), thus, demonstrating the strong link between the updraft dynamics and hail formation.
316 Furthermore, the total hydrometeor mixing ratio (Fig. 4a) is consistent with the number concentrations from both rain and
317 hail (Figs. 4e and 4f).

318 Figures 5a,d,g (left column in Fig. 5) show simulated reflectivity, Z_{DR} , and K_{DP} , respectively, averaged over the region
319 with reflectivity $> 40 \text{ dBZ}$ from the original, cartesian model grid. The evolution of raindrops as represented by rain D_m
320 (Fig. 4c) is evident by the large values in the Z_{DR} field (Fig. 5d). The relatively large K_{DP} and reflectivity values also seem

321 to accurately represent the high number concentration of raindrops in the early stage of the cell lifetime (Figs. 4e and 5a,g).
322 These characteristics of reflectivity, Z_{DR} , and K_{DP} are compared with those from the different scan strategies: 1-min RHI
323 (middle column) and 5-min VCP (right column). The RHI tracking reconstructs the magnitudes and evolution of the
324 polarimetric observables well (Figs. 5e and 5h) so that they represent the hail D_m and cell evolution (Figs. 4a,b,d).
325 Meanwhile, the conventional volume scan cannot capture the fine-scale structure and magnitudes of the hail-rain evolution
326 observed by Z_{DR} and K_{DP} (Figs. 5f and 5i) due to the coarse time resolution. The RHI tracking performs well in capturing
327 the K_{DP} enhancement and its streak as the raindrops fall (Fig. 5h). Note that the NEXRAD S-band frequency (3.0 GHz) is
328 assumed for the 5-min VCP simulation, while C-band frequency (5.5 GHz) is assumed for the model and RHI simulation.
329 Therefore, the K_{DP} values in this figure do include the frequency dependency. The S-band K_{DP} (Fig. 5i) is approximately
330 1.8 (5.5 GHz/3.0 GHz) times smaller than the C-band K_{DP} (Fig. 5h). This indicates that the K_{DP} measurements from the
331 shorter-wavelength radar are more sensitive to the K_{DP} evolution, and therefore, can provide more insights on the
332 microphysical evolution of precipitation.

333 The region of relatively large $Z_{DR} > 1$ dB extends to 6 km altitude, which is approximately 1 km above the environmental
334 0°C level (horizontal dashed line) at around 21:38 UTC (Figs. 5d and 5e). This seems to correspond to the so-called Z_{DR}
335 column (e.g., Kumjian et al., 2014). The Z_{DR} column signature shows more columnar structure in the vertical cross section
336 at 21:38 UTC (not shown). The Z_{DR} extension is clearly evident in the original model simulation (truth) (Fig. 5d) and the
337 RHI tracking (Fig. 5e), but it is not clear or is weak in 5-min VCP (Fig. 5f). The large Z_{DR} values associated with raindrops
338 can be masked by the presence of hail. Hail particles are assumed to be dry and more near-spherical than raindrops following
339 Ryzhkov et al. (2011) in CR-SIM and dominate the total reflectivity, producing smaller Z_{DR} . The Z_{DR} extension is collocated
340 with large $K_{DP} > 1.8 \text{ }^\circ \text{ km}^{-1}$ shown in the original model simulation truth (Fig. 5g) and the RHI tracking (Fig. 5h).

341 **3.3 Dynamical evolution**

342 One of the benefits of cell tracking using VIL is that it can better capture the dynamical evolution of convective cells
343 over their lifetimes (Fig. 2). Figure 6 represents the maximum updrafts in the CLN and POL individual tracked cells as a
344 function of their lifetime for deep convective cells with 20 dBZ echo top heights exceeding the environmental 0°C level.
345 Many of the cells attain maximum updrafts $> 10 \text{ m s}^{-1}$ within the first third of their lifetimes in both the CLN and POL
346 simulations. The peak occurrence for the POL simulation is found for updrafts that are approximately 5 m s^{-1} stronger than
347 those of the CLN simulation, suggesting that stronger updrafts are more frequent in the POL than CLN convective cells in
348 the earlier stages of the cells' lifecycles. Since the earlier stages of convection are driven by warm-phase processes, this
349 finding is consistent with Marinescu et al. (2021), who found stronger updrafts in the warm-phase region of deep convective
350 updrafts, but not in the cold-phase region (i.e., above the freezing level) in the POL environment. The stronger updrafts
351 support the development of larger hail produced in the POL simulation (not shown). This result suggests that it is important
352 to estimate vertical velocity with a high level of accuracy if the impact of aerosols on convective dynamics is to be properly

353 resolved in observations. We use the CLN simulation output as well as the individual CLN case deep convective cell shown
354 in Figs. 4 and 5 to further investigate the uncertainties associated with the multi-Doppler radar vertical velocity retrievals
355 in this section. Figure 7 shows the maximum updraft velocity in the cell column at each time as a function of the normalized
356 lifetime for the nine deep convective cells from the CLN simulation selected in the previous section. They all have peak
357 updrafts exceeding 20 m s^{-1} , which mostly occur in the first half of the cells' lifetimes. The black line represents the profile
358 from the target cell analyzed for the OSSE in this section. It is clear from Figure 7 that the selected cell has a relatively
359 typical dynamical evolution when compared with the other nine cells, although it does reach its maximum updraft velocity
360 a little earlier in its lifecycle.

361 Figure 8 shows the impacts of sets of radar scan strategies for multi-Doppler updraft retrievals for the selected convective
362 cell using a 3DVAR technique (North et al., 2017; Oue et al., 2019). This cell is the same cell examined in the previous
363 section (Figs. 4 and 5). We simulate different combinations of the scan strategies using 1-min RHI that scans around the
364 center of the cell and 5-min VCP. Recall, Table 1 provides the details of the scan strategies, and Figure 1 shows the locations
365 of the radars with these scan strategies and the targeted OSSE cell. The sets of radars for the multi-Doppler wind retrieval
366 simulations are: 1) two radars, each using a 1-min RHI (red dot and cross in Fig. 1, called 2RHI); 2) two radars, each using
367 a 5-min VCP (called 2VCP); 3) two radars, with one using a 1-min RHI (red dot in Fig. 1) and the other using a 5-min VCP
368 (red cross in Fig. 1) (called RHIVCP); and 4) three radars, with two using 1-min RHIs (red and blue dots in Fig. 1) and one
369 using a 5-min VCP (red cross in Fig. 1) (called 2RHIVCP). Table 2 represents the root mean square errors (RMSEs) of the
370 retrieved vertical velocity at four different heights, as well as at all heights. The 2VCP simulation (Figure 8c; green in Figure
371 8f) significantly underestimates the updraft, with the error exceeding 5 m s^{-1} above 5 km AGL, where the cell produces
372 mean updrafts stronger than 12 m s^{-1} . The 2VCP radar pair, whose volume scan takes 5 minutes, does not resolve the updraft
373 evolution well. We note that other studies also found an underestimation of vertical velocity retrievals using two 5-min
374 VCPs. For example, Marinescu et al. (2020) used two 5-min VCPs to estimate strong updrafts in supercells and found an
375 underestimation in the region from 5-10 km AGL when compared with radiosonde estimates of vertical velocity. This pair
376 of 5-min VCPs (2VCP) does, however, produce less error below 4 km AGL where the cell produces weaker updrafts (< 5
377 m s^{-1}) when compared with the other sets of radar combinations. This suggests that the conventional PPI scans, which have
378 dense scans at low elevation angles, well capture the low-level horizontal inflow, and the mass continuity assumption is
379 well satisfied at the low levels. It is interesting that while 5-min VCP represents VIL well for the distance $> 30 \text{ km}$ as shown
380 in Fig. 3, its limitations produce significant uncertainties in the convective dynamical retrieval of individual clouds above
381 $\sim 5 \text{ km}$ AGL even though the cell is observed at a distance $> 30 \text{ km}$ from the radar (Fig. 1).

382 With an RHI scan every minute, even when adding only one RHI, cell tracking improves the retrievals above 5 km altitude
383 (Figs. 8b,d,e; 2RHI, RHIVCP, and 2RHIVCP; red, magenta, and blue, respectively in Figure 8f). The improvements are
384 particularly significant for regions in which the updraft velocities are stronger than 10 m s^{-1} . The RHIVCP simulation shows
385 the best estimate at the middle altitude ($\sim 6 \text{ km}$) among the four simulations, followed by 2RHIVCP, and thirdly 2RHI. The

386 2RHI and 2RHIVCP simulations show RMSEs less than 6 m s^{-1} at all altitudes and better estimates than the other two
387 simulations at the higher altitudes (8 and 10 km AGL). The RHI scan has better sampling in the higher elevations than 5-
388 min VCP, resulting in a better retrieval at these higher altitudes.

389 As the profile and Table 2 show, 2RHI and 2RHIVCP have the lowest RMSEs when considering all altitudes (Table 2,
390 bottom row). In addition, 2RHIVCP shows better results at altitudes $< 10 \text{ km}$ than 2RHI. This suggests that the conventional
391 5-min VCP scan can be used for further improvement of the RHI-only tracking retrievals for the low and middle altitudes.
392 Since the 5-min VCP has dense scans at lower elevations, this can help to provide enough data covering the horizontal
393 domain of the cell, which may better represent the low-level horizontal wind convergence, thereby, better constraining the
394 cost functions in the 3DVAR.

395 We also investigate the impacts of the radar radial locations relative to the same cell as in Figs. 4, 5 and 8. Radars
396 horizontally extending from 10 to 70 km (in 10 km increments) radially away from the cell are assessed. For this analysis,
397 we use the scan strategy with the lowest errors from our prior analysis, i.e., two radars performing 2-min SECs and one
398 radar performing 5-min VCP (e.g., Table 2, the tracking radars used 2-min SEC rather than 1-min RHI, We believe that 1-
399 min RHI can be feasible with electrical scan or mechanical rapid scan radars. However, 2-min SEC can be more reasonable
400 when the cell is relatively close to the radars, because scans need to extend to higher elevations as discussed in Sect. 2.4.2).
401 Figure 9a shows the radar locations for the seven simulations and Figure 9b demonstrates the vertical profiles of errors of
402 the retrieved updrafts averaged over a $20 \text{ km} \times 20 \text{ km}$ box with reflectivity $> 30 \text{ dBZ}$ at 21:42 UTC. For each retrieval, the
403 largest error is evident above an altitude of $\sim 9 \text{ km AGL}$ where the stronger updrafts are simulated by the model (Fig. 8a).
404 The largest error among the retrievals is found in the retrieval with the radars closest to the cell (red profile in Fig. 9b). This
405 occurs since the PPI volume scan does not cover the upper part of the cell and/or the horizontal wind convergence at higher
406 elevation angles may not be retrieved from the RHI measurements accurately. When each radar has a distance greater than
407 or equal to 20 km from the cell, the retrievals are improved by $5\text{-}10 \text{ m s}^{-1}$ between 5 to 11 km altitudes. The retrievals in
408 which the radar distances from the cell fall between 20 and 50 km show errors less than 5 m s^{-1} below 11 km AGL. Such
409 accuracies in the retrievals may allow for resolving the aerosol impacts on updraft velocities shown in Fig. 6. The errors are
410 then found to increase again above 10 km AGL, especially for the radars located 60 and 70 km away from the cell. This
411 investigation suggests that the radars should target cells that are between 20-50 km from the radar for optimal multi-Doppler
412 radar retrievals. This finding is consistent with previous field campaigns using multi-Doppler radar measurements (e.g.,
413 Wurman et al., 2012; Collis et al., 2013; Jensen et al., 2016) and OSSE studies (e.g., Potvin et al., 2012a).

414 In the simulations above, the three radar locations are almost equidistant from the target cell. Now we explore the
415 impacts of having radars located at different distances from the target. We move one of the three radars to a distance of 10
416 to 70 km at 10 km increments (except 20 km which has already been tested) while keeping the other two radars as a fixed
417 distance of 20 km (blue dots in Fig. 9a). Similar to Fig. 9b, Figs. 10a and 10b show vertical profiles of the errors of the
418 retrieved updrafts when moving the 2-min SEC radar (at the northwest corner of the triangle) and the 5-min VCP radar (at

419 the south corner), respectively. When moving the 2-min SEC radar from distances between 30 and 70 km (Fig. 10a), the
420 retrievals show better profiles as the RMSEs range from 1.7 to 2.6 m s⁻¹. The RMSE increases when the radar is located at
421 10 km, which is consistent with the equidistance simulations (Fig. 9). Another notable point is that when the radar is located
422 at distances from 50 to 70 km, the errors below 1 km slightly increase, which is most likely because the radar coverage is
423 sparse at the lowest elevation due to the distance. Similarly, when moving the 5-min VCP radar, the RMSE increases when
424 the radar is located at 10 km (Fig. 10b). The impact is significant above 5 km altitude. When the radar is located at 60 or 70
425 km the errors below 5 km increase. This also reflects the sparse radar coverage at the lower altitudes for the far distances.

426 In nature, convective cells often do not nicely evolve over pre-defined multi-Doppler regions and move outside the
427 region of optimal analysis. Therefore, we also propose a single-RHI vertical velocity retrieval which can be used on a much
428 larger sample of convective cells in the vertical in the vicinity of the radar compared to fixed, multi-Doppler platforms. The
429 single-RHI vertical velocity retrieval extracts the vertical air motion component from the radial velocity (Doppler velocity)
430 which is composed of the vertical air motion, horizontal air velocity, and hydrometeor fall velocity (Lamer et al., 2014).
431 Figure 11a shows examples of Doppler velocity vectors (clear arrows) and the components of the Doppler velocity including
432 horizontal wind along the RHI plane (yellow arrows), vertical velocity (red arrows), and hydrometeor fall velocity (blue
433 arrows) at two different points ($[x,y]=[0 \text{ km}, 5 \text{ km}]$ and $[7.5 \text{ km}, 5 \text{ km}]$). These examples assume that each component at
434 the two points has the same value. At the radar distance equal to 0 km ($x=0 \text{ km}$), the horizontal wind component can be
435 ignored. At the radar distance greater than 0 km, the contribution of the horizontal wind component increases with
436 decreasing elevation angle (i.e., increasing the distance from the radar at a constant height). To apply this technique to real
437 observations, horizontal velocity and hydrometeor fall velocity should be provided. Generally, the horizontal velocity profile
438 can be provided from a velocity-azimuth display (VAD) technique using PPI measurements or sounding measurements,
439 assuming that the horizontal wind is constant at each level. However, this assumption is a major source of the uncertainty
440 in the single-RHI vertical velocity retrieval technique, particularly at lower elevation angles. At these lower elevation angles,
441 the horizontal wind component dominates the radial velocity, but the coverage of these lower elevation angles often does
442 not properly capture the variability in the horizontal wind, especially close to the radar. We, therefore, investigate the impact
443 of the distance of the radar from the cell on the single-RHI retrieval. In the simulations, we use the reflectivity-weighted
444 hydrometeor fall velocity simulated by CR-SIM, similar to the present multi-Doppler retrieval simulations, to exclude the
445 uncertainty related to the fall velocity estimates.

446 Figure 11 shows the simulated single RHI vertical velocity retrieval from the selected convective cell. Profiles in Figs.
447 11c and 11d are retrieved vertical velocity at the convective core (distance = 0 km) and the errors from the truth, respectively.
448 We investigate this technique for a profile at 21:42 UTC of the cell (same as Figs. 8f and 9b), where the strongest updraft
449 is simulated. This single-RHI Doppler velocity technique works very well at the distance = 0 km (red), where the horizontal
450 wind component can be ignored, as evidenced by the error profile being equal to 0 at all altitudes (red line). However, below
451 6 km AGL, the error significantly increases with the radar distance from the core. Interestingly, the characteristics of the
452 error distribution are opposite to those of the multi-Doppler retrievals (Figs. 8f and 9b). We would, therefore, suggest the

453 complementary use of the multi-Doppler wind retrieval and the single-RHI vertical velocity retrieval for better vertical
454 velocity estimates of convective cells. For example, in a tracking strategy in which two radars track a targeted cell, the
455 optimal scenario can be one in which the two radars track the cell with sector RHI/PPI scans at intervals of ~ 2 min when
456 the distance of the cell from both radars is greater than 20 km. However, when the distance of the cell from one of the radars
457 is less than 20 km, the radar's scan is then switched to hemispheric RHI.

458 This study highlights the importance of focusing on high-spatiotemporal observations of individual convective cells
459 rather than utilizing conventional surveillance scans. Such high-spatiotemporal observations can be accomplished by
460 tracking cells using fast scan RHI measurements facilitated by rapid-scan radars. However, it is not hard to anticipate that
461 the number of individual cells tracked successfully during a short-term intensive observation period where such special scan
462 strategies are performed will also be limited. Therefore, we have investigated the sample size of cells needed to represent
463 the typical convective evolution of deep convective cells using the median maximum updraft metric shown in Fig. 6. This
464 specific analysis accounts for the error regarding cell sampling, but it does not account for the wind retrieval uncertainty
465 from the scan strategy. Figures 12a and 12c show boxplots of the maximum vertical velocity as a function of the normalized
466 lifetime from all convective cells detected (910 tracked cells including deep and shallow cells) in the CLN case and from
467 deep convective cells defined in Fig. 6a (453 tracked cells), respectively. These figures indicate high variability in the
468 maximum updraft magnitude as a function of time, and that potentially, one randomly sampled convective cell may not
469 represent the typical evolution of vertical velocity. Figure 12b depicts the relationship between the sample size and the
470 errors associated with estimating the full population median evolution of the maximum updraft magnitude. We randomly
471 sample convective cells from all of the *tobac*-detected cells in the CLN simulation (910 tracked cells) and estimate the
472 median value of maximum updrafts at each time bin with different numbers of samples. The median values for the different
473 sample sizes are then compared to the median values from all deep convective cells detected (shown as a black line in Fig.
474 6a) to estimate RMSEs. Figure 12b suggests that increasing the sample size generally decreases the RMSE to less than 4.5
475 m s^{-1} until a population of 10 cell samples is reached and converges to approximately 2.6 m s^{-1} for a sample size of 20 or
476 more samples. When focusing the analysis on deep convective cells only (Fig. 12d), the RMSE decreases to approximately
477 3 m s^{-1} for 10 cell samples and converges to approximately 1 m s^{-1} for 40 or more samples.

478 This study focuses on tracking isolated deep convective cells, each of which has a single core. Although we provide a
479 detailed investigation of one selected cell using OSSEs, the result should be robust for the other cells that have a similar
480 vertical structure to that shown in Sect. 3.2. The error values presented in this study, however, may depend on cloud type.
481 As the larger errors of the multi-Doppler radar wind retrievals are shown to exist in the higher altitudes in this study, the
482 heights of convection could influence the observational uncertainties (i.e., height of maximum updraft). Moreover, in a
483 strong wind shear environment where storms advect quickly, the impact of the use of quick updates of RHI scans would be
484 more effective (e.g., Clark et al., 1980; Oue et al., 2019). Various convective cloud morphologies have been investigated in
485 terms of uncertainties in observations, including mesoscale convective systems (e.g., Bousquet et al., 2008; Oue et al.,
486 2019), supercells (e.g., Potvin et al., 2012; Marinescu et al., 2020), and convection embedded in stratiform precipitation

487 (e.g., Bousquet et al., 2008). However, the qualitative characteristics found in this study, such as the error profile trends, the
488 dependency on the radar locations, and the dependency on scan strategy, are likely to be common to those deep convective
489 cloud systems, as well.

490

491 **4 Summary**

492

493 Optimizing radar observation strategies has been one of the most important topics in pre-field-campaign periods,
494 especially when the focus is on atmospheric phenomena that rapidly evolve on timescales that standard operational radar
495 networks cannot resolve. This study uses the Cloud-resolving Radar Simulator (CR-SIM) and the *tobac* cloud object
496 tracking algorithm to investigate observational uncertainties of isolated deep convective clouds associated with pre-existing
497 and planned radar deployments and strategies. The focus of this manuscript is to optimize the radar observation strategies
498 for the TRACER/ESCAPE field campaign, but the results are also generalizable for field campaigns that focus on isolated
499 deep convection using radar observations.

500 The following results and associated recommendations are made:

- 501 ● The cell tracking algorithm with the use of VIL better captures the difference in cell lifetimes between the low-CCN
502 (CLN) and high-CCN (POL) simulations compared with the use of reflectivity thresholds at individual altitudes and
503 is suitable to detect and track more convective cells for longer time periods, including the early-developing and
504 dissipating stages of isolated storms.
- 505 ● An analysis of the CLN and POL simulations, used to quantify the impact of aerosols on the convective dynamical
506 evolution, show a 5-7 m s^{-1} difference in maximum updraft at the early stages of convective development. This
507 suggests the importance of accurate vertical velocity estimates using the radar observations if the impact of aerosols
508 on convective updrafts is to be assessed.
- 509 ● Fast scanning of the individual convective cells every minute captures the microphysical evolution better than the
510 operational radar observations that update the volume scan every 5 min. In particular, the tracking of cells using RHI
511 every minute better captures the evolution of K_{DP} in the early stage and Z_{DR} in the later stage, which are primarily
512 associated with the rain number concentration and hydrometeor particle (hail and rain) size, respectively.
- 513 ● Tracking using RHI improves the multi-Doppler radar updraft retrievals above 5 km AGL, particularly for regions
514 with updraft velocities greater than 10 m s^{-1} . The conventional 5-min PPI volume scan can be used for further
515 improvement of the RHI-tracking-only retrievals.
- 516 ● The multi-Doppler radar updraft retrievals, even when using RHI, are still challenging, especially for cells that are
517 close to the radars (i.e., within 10 km of the radar). This approach can be complemented by a single RHI updraft
518 retrieval technique.
- 519 ● Based on these results, the suggested strategy to better capture microphysics and dynamics of deep convective cells
520 is tracking by frequent RHI scans from more than one radar (blue and red scans in Fig. 13), in addition to the

521 operational PPI volume scans generally performed by the NEXRAD radars (green scans in Fig. 13). We also suggest
522 a hybrid radar scan strategy which switches between the RHI cell tracking and hemispheric RHI measurements
523 depending on the distance between the radar and the targeted cell (red and orange scans in Fig. 13). Such RHI tracking
524 measurements would be possible with conventional mobile radars, but the fast-scanning Doppler radars (Wurman,
525 2001), and/or phased array radars (Kollias et al., 2022) would have more advantages in faster updating, better spatial
526 resolution, and higher quality datasets.

- 527 • Increasing the number of deep convective cells sampled by such observations better represents the population median
528 maximum updraft evolution. When increasing the number of deep cells sampled to more than 10, the RMSE
529 decreases to less than 3 m s^{-1} , and when increasing the sample size to more than 40, the RMSE further decreases to
530 less than 1 m s^{-1} .

531

532 For the strategy suggested above we have assumed that the real-time cell tracking will be guided by another algorithm
533 that will take advantage of surveillance scans by conventional radar networks (e.g., a Multi Sensor Agile Adaptive Sampling
534 (MAAS) framework (Kollias et al., 2020). The new MAAS has incorporated a cell-tracking algorithm using a watershed
535 technique (similar to *tobac* and the approach of Hu et al., 2019) and predicts the future location of convective cells using
536 multiple sensors (e.g., NEXRAD radar at Houston, TX and GOES-16).

537 Finally, this study highlights the importance of using OSSEs in developing radar strategies during pre-field campaign
538 periods. Current radar systems used for field campaigns, as well as operational radars, have more functions (e.g.,
539 polarimetry, Doppler, Doppler spectrum, and dual wavelength) and configurable parameters (e.g., pulse sampling, pulse
540 width, range-bin gate, azimuth, elevation spacings) than in the past. While this increased functionality makes the scan
541 strategies more sophisticated, it also makes the optimization of the scan strategy more complex. Although we argue that the
542 results from this study can be applied to other field campaigns that focus on deep convection, for more qualitative analyses,
543 the pre-field campaign OSSEs should also be optimized for a specific field campaign thereby accounting for characteristics
544 of the radar systems that will be used for the field campaigns. The use of a radar simulator in the OSSEs provides several
545 advantages including 1) facilitating instrument deployments, such as the radar locations and the number of radars required,
546 and accounting for the radar characteristics and functions; 2) optimizing radar configurations such as the scan rate, elevation
547 angles, update time of scans, and trade-offs; and 3) quantifying errors of the observables and retrievals. Effective OSSEs
548 can lead to successful, state-of-the-art field campaigns and provide high-quality, unique datasets that can allow for new
549 insights of the atmospheric phenomena.

550

551

552 **Code availability.** The source code and user manual for the Cloud Resolving Model Radar Simulator (CR-SIM) are available
553 at <https://www.bnl.gov/CMAS/cr-sim.php>, last access: 21 April 2022, and those for Tracking and Object-Based Analysis
554 of Clouds (*tobac*) are available at <https://tobac.readthedocs.io/en/latest/>.

555

556 **Data availability.** The ACPC model intercomparison project deep convection simulation data used for the input of CR-SIM
557 are stored and can be accessed on the U.K. CEDA JASMIN supercomputer. Vertically integrated liquid (VIL) products
558 from CR-SIM used for the convective cell tracking are available in Stony Brook University Academic Commons
559 (<https://commons.library.stonybrook.edu/somasdata/16>, last access July 29, 2022).

560

561 **Author contributions.** The radar simulator and cell tracking work and analysis were made by MO. Conceptualization of the
562 method, interpretation, and writing were shared between MO, PK, SMS, PJM, and SCV. The radar simulator was developed
563 by MO and PK's group, and the cell tracking code was developed by SCV's group.

564

565 **Competing interests.** The authors declare that they have no conflict of interest.

566

567 **Acknowledgements.**

568 M. Oue, S. M. Saleeby, and S. C. van den Heever were supported by Atmospheric System Research (grant no. DE-
569 SC0021160). M. Oue and P Kollias were also supported by National Science Foundation Grant FAIN-2019932.

570

571

572

- 574 Adachi, T., and Mashiko, W.: High temporal-spatial resolution observation of tornadogenesis in a shallow supercell
575 associated with Typhoon Hagibis (2019) using phased array weather radar. *Geophys. Res. Lett.*, 47, e2020GL089635.
576 <https://doi.org/10.1029/2020GL089635>, 2020.
- 577 Barnes, S. L.: A Technique for maximizing details in numerical weather map analysis, *J. Appl. Meteorol.*, 3, 396–409,
578 1964. Billam, E.R. and D.H. Harvey. 1987. MESAR—An advanced experimental phased array radar. Proceedings of
579 the IEEE International Radar Conference, London, 37–40.
- 580 Bousquet, O., Tabary, P., and Parent du Chatelet, J.: Operational multiple-Doppler wind retrieval inferred from long-
581 range radial velocity measurements, *J. Appl. Meteor. Climatol.*, 47, 2929–2945,
582 <https://doi.org/10.1175/2008JAMC1878.1>, 2008.
- 583 Bryan, G. H., and Fritsch, J. M.: A benchmark simulation for moist nonhydrostatic numerical models. *Monthly Weather*
584 *Review*, 130, 2917–2928, 2002.
- 585 Clark, T. L., Harris, F. I., and Mohr, C. G.: Errors in wind fields derived from multiple-Doppler radars: Random errors
586 and temporal errors associated with advection and evolution, *J. Appl. Meteorol.*, 19, 1273–1284, 1980.
- 587 Collis, C., Protat, A., May, P. T., and Williams, C.: Statistics of storm updraft velocities from TWP-ICE including
588 verification with profiling measurements, *J. Appl. Meteor. Climatol.*, 52, 1909–1922, [https://doi.org/10.1175/JAMC-](https://doi.org/10.1175/JAMC-D-12-0230.1)
589 [D-12-0230.1](https://doi.org/10.1175/JAMC-D-12-0230.1), 2013.
- 590 Collis, S., Protat, A., and Chung, K.-S.: The effect of radial velocity gridding artifacts on variationally retrieved vertical
591 velocities, *J. Atmos. Ocean. Tech.*, 27, 1239–1246, 2010.
- 592 Cotton, W. R., and Coauthors: RAMS 2001: Current status and future directions. *Meteor. Atmos. Phys.*, 82, 5–29,
593 <https://doi.org/10.1007/s00703-001-0584-9>, 2003.
- 594 Given, T. and Ray, P. S.: Response of a two-dimensional dual-Doppler radar wind synthesis, *J. Atmos. Ocean. Tech.*, 11,
595 239–255, [https://doi.org/10.1175/1520-0426\(1994\)011<0239:ROATDD>2.0.CO;2](https://doi.org/10.1175/1520-0426(1994)011<0239:ROATDD>2.0.CO;2), 1994.
- 596 Fridlind, A. M., van Lier-Walqui, M., Collis, S., Giangrande, S. E., Jackson, R. C., Li, X., Matsui, T., Orville, R., Picel,
597 M. H., Rosenfeld, D., Ryzhkov, A., Weitz, R., and Zhang, P.: Use of polarimetric radar measurements to constrain
598 simulated convective cell evolution: a pilot study with Lagrangian tracking, *Atmos. Meas. Tech.*, 12, 2979–3000,
599 <https://doi.org/10.5194/amt-12-2979-2019>, 2019.
- 600 Griffin, C. B., Bodine, D. J., Kurdzo, J. M., Mahre, A., and Palmer, R. D.: High-temporal resolution observations of the
601 27 May 2015 Canadian, Texas tornado using the Atmospheric Imaging Radar. *Mon. Wea. Rev.*, 147, 873 – 891, 2019.
- 602 Heikenfeld, M., Marinescu, P. J., Christensen, M., Watson-Parris, D., Senf, F., van den Heever, S. C., and Stier, P.: Tobac
603 1.2: Towards a flexible framework for tracking and analysis of clouds in diverse datasets. *Geosci. Model Dev.*, 12,
604 4551–4570, <https://doi.org/10.5194/gmd-12-4551-2019>, 2019. Heinselman, P. L., and Torres, S. M.: High-temporal-

605 resolution capabilities of the national weather radar testbed phased-array radar. *J. Appl. Meteor. Climatol.*, 50, 579-
606 593, 2011.

607 Hu, J., Rosenfeld, D., Zrnich, D., Williams, E., Zhang, P., Snyder, J. C., Ryzhkov, A., Hashimshoni, E., Zhang, R., Weitz,
608 R.: Tracking and characterization of convective cells through their maturation into stratiform storm elements using
609 polarimetric radar and lightning detection, *Atmospheric Research*, 226, 192-207, 2019,
610 <https://doi.org/10.1016/j.atmosres.2019.04.015>.

611 Jensen, M., Bruning, E., Collins, D., Fridlind, A., Kollias, P., Kuang, C., Rosenfeld, D., Ryzhkov, A., Varble, A., Brooks,
612 S.D., Collis, S., Defer, E., Fan, J., Flynn, J., Giangrande, S., Griffin, R., Hu, J., Jackson, R., Kumjian, M., Logan, T.,
613 Matsui, T., McFarquhar, G., Nowotarski, C., Quaas, J., Oue, M., Sheesley, R., Snyder, J., Stier, P., Usenko, S., van den
614 Heever, S., van Lier Walqui, M., Wang, Y., Xu, Y., and Zhang, G.: Tracking Aerosol Convection Interactions
615 ExpeRiment (TRACER) Science Plan. Ed. by Robert Stafford, DOE/SC-ARM-19-017, 2019.

616 Jensen, M. P., Petersen, W. A., Bansemer, A., Bharadwaj, N., Carey, L. D., Cecil, D. J., Collis, S. M., Del Genio, A. D.,
617 Dolan, B., Gerlach, J., Giangrande, S. E., Heymsfield, A., Heymsfield, G., Kollias, P., Lang, T. J., Nesbitt, S. W.,
618 Neumann, A., Poellot, M., Rutledge, S. A., Schwaller, M., Tokay, A., Williams, C. R., Wolff, D. B., Xie, S., & Zipser,
619 E. J. (2016). The Midlatitude Continental Convective Clouds Experiment (MC3E), *Bulletin of the American
620 Meteorological Society*, 97(9), 1667-1686.

621 Jensen, M. P., Flynn, J. H., Judd, L. M., Kollias, P., Kuang, C., Mcfarquhar, G., Nadkarni, R., Powers, H., & Sullivan, J.
622 (2022). A Succession of Cloud, Precipitation, Aerosol, and Air Quality Field Experiments in the Coastal Urban
623 Environment, *Bulletin of the American Meteorological Society*, 103(2), 103-105.

624 Kang, C., Giangrande, S.E., Serbin, S. P., Campbell, P., Hickmon, N., Ritsche, M. 2021: Science and Deployment Plan
625 for the DOE 3rd Atmospheric Radiation Measurement Mobile Facility in the Southeastern United States, 2021 AGU
626 Fall Meeting, New Orleans and Online, 13 – 17 December 2021, online available at
627 https://www.arm.gov/uploads/2021_AGU_SE_US_TownHall_Slides.pdf

628 Khairoutdinov, M. F., and Randall, D.A.: Cloud-resolving modeling of the ARM summer 1997 IOP: Model formulation,
629 results, uncertainties and sensitivities. *J. Atmos. Sci.*, 60, 607-625, 2003.

630 Kollias, P., Luke, E., Oue, M., & Lamer, K. (2020). Agile adaptive radar sampling of fast-evolving atmospheric
631 phenomena guided by satellite imagery and surface cameras. *Geophysical Research Letters*, 45, e2020GL088440.
632 <https://doi.org/10.1029/2020GL088440>

633 Kollias, P., Luke, E., Oue, M., and Lamer, K.: Agile adaptive radar sampling of fast-evolving atmospheric phenomena
634 guided by satellite imagery and surface cameras. *Geophysical Research Letters*, 45, e2020GL088440.
635 <https://doi.org/10.1029/2020GL088440>, 2020.

636 Kollias, P., Luke, E., Tuftedal, K., Dubois, M. Knapp, E.J. : Agile Weather Observations using a Dual-Polarization X-
637 band Phased Array Radar. *IEEE Radar Conference New York, NY.,2022.*

638 Kumjian, M. R., and Ryzhkov, A. V.: Polarimetric signatures in supercell thunderstorms. *J. Appl. Meteor. Climatol.*, **47**,
639 1940–1961, doi:10.1175/2007JAMC1874.1, 2008

640 Kumjian, M. R., Khain A. P. , Benmoshe N. , Ilotoviz E. , Ryzhkov A. V. , and Phillips V. T. J.: The anatomy and physics
641 of ZDR columns: Investigating a polarimetric radar signature with a spectral bin microphysical model. *J. Appl. Meteor.*
642 *Climatol.*, **53**, 1820–1843, doi:10.1175/JAMC-D-13-0354.1. 2014.

643 L’Ecuyer, T., Petersen, W., and Moiseev, D.: Light Precipitation Validation Experiment (LPVEx) Science Plan. NASA,
644 2010, available at https://ghrc.nsstc.nasa.gov/home/sites/default/files/lpvex_science_plan_June2010.pdf, last access on
645 July 11th, 2022.

646 Mahre, A., Kurdzo, J. M., Bodine, D. J., Griffin, C. B., and Palmer, R. D.: Analysis of the 16 May 2015 Tipton,
647 Oklahoma, EF-3 tornado at high spatiotemporal resolution using the Atmospheric Imaging Radar. *Mon. Wea. Rev.*,
648 146, 2103 – 2124, 2018.

649 Marinescu, P. J., Kennedy, P. C., Bell, M. M., Drager, A. J., Grant, L. D., Freeman, S. W., and van den Heever, S. C.:
650 Updraft vertical velocity observations and uncertainties in High Plains supercells using radiosondes and radars. *Mon.*
651 *Wea. Rev.*, 148, 4435–4452, 2020, <https://doi.org/10.1175/MWR-D-20-0071.1>.

652 Marinescu, P. J., van den Heever, S. C., Heikenfeld, M., Barrett, A. I., Barthlott, C., Hoose, C., Fan, J., Fridlind, A. M.,
653 Matsui, T., Miltenberger, A. K., Stier, P., Vie, B., White, B. A., and Zhang, Y. : Impacts of Varying Concentrations of
654 Cloud Condensation Nuclei on Deep Convective Cloud Updrafts—A Multimodel Assessment, *Journal of the*
655 *Atmospheric Sciences*, 78(4), 1147-1172, 2021.

656 McLaughlin, D. J., V. Chandrasekar, K. Droegemeier, S. Frasier, K. Kurose, F. Junyent, B. Philips, S. Cruz-Pol, and J.
657 Colom: Distributed Collaborative Adaptive Sensing (DCAS) for Improved Detection, Understanding, and Prediction
658 of Atmospheric Hazards. Presented at Ninth Symposium on Integrated Observing and Assimilation Systems for the
659 Atmosphere, Oceans, and Land Surface (IOAS-AOLS), American Meteorological Society. Boston, MA: American
660 Meteorological Society, 2005.

661 Mishra, K. V., Krajewski, W. F., Goska, R., Ceynar, D., Seo, B., Kruger, A., Niemeier, J. J., Galvez, M. B., Thurai, M.,
662 Bringi, V. N., Tolstoy, L., Kucera, P. A., Petersen, W. A., Grazioli, J., and Pazmany, A. L.: Deployment and
663 Performance Analyses of High-Resolution Iowa XPOL Radar System during the NASA IFloodS Campaign, *Journal of*
664 *Hydrometeorology*, 17(2), 455-479, 2016. ModEx Approach - Environmental System Science Program, U.S. DOE
665 Environmental System Science Program, <https://ess.science.energy.gov> (accessed [May 11, 2022])

666 North, K. W., Oue, M., Kollias, P., Giangrande, S. E., Collis, S. M., and Potvin, C. K.: Vertical air motion retrievals in
667 deep convective clouds using the ARM scanning radar network in Oklahoma during MC3E, *Atmos. Meas. Tech.*, 10,
668 2785–2806, <https://doi.org/10.5194/amt-10-2785-2017>, 2017.

669 Oue, M., Kollias, P., Shapiro, A., Tatarevic, A., and Matsui, T.: Investigation of observational error sources in multi-
670 Doppler-radar three-dimensional variational vertical air motion retrievals, *Atmos. Meas. Tech.*, 12, 1999–2018,
671 <https://doi.org/10.5194/amt-12-1999-2019>, 2019.

672 Oue, M., Tatarevic, A., Kollias, P., Wang, D., Yu, K., and Vogelmann, A. M.: The Cloud-resolving model Radar
673 Simulator (CR-SIM) Version 3.3: description and applications of a virtual observatory, *Geosci. Model Dev.*, 13, 1975–
674 1998, <https://doi.org/10.5194/gmd-13-1975-2020>, 2020.

675 Potvin, C. K., Betten, D., Wicker, L. J., Elmore, K. L., and Biggerstaff, M. I.: 3DVAR versus traditional dual-Doppler
676 wind retrievals of a simulated supercell thunderstorm, *Mon. Weather Rev.*, 140, 3487–3494,
677 <https://doi.org/10.1175/MWRD-12-00063.1>, 2012a.

678 Potvin, C. K., Wicker, L. J., and Shapiro A.: Assessing errors in variational dual-Doppler wind syntheses of supercell
679 thunderstorms observed by storm-scale mobile radars, *J. Atmos. Ocean. Tech.*, 29, 1009–1025,
680 <https://doi.org/10.1175/JTECHD-11-00177.1>, 2012b.

681 Powers, J. G., Klemp, J. B., Skamarock, W. C., Davis, C. A., Dudhia, J., Gill, D. O., Coen, J. L., Gochis, D. J., Ahmadov,
682 R., Peckham, S. E., Grell, G. A., Michalakes, J., Trahan, S., Benjamin, S. G., Alexander, C. R., Dimego, G. J., Wang,
683 W., Schwartz, C. S., Romine, G. S., Liu, Z., Snyder, C., Chen, F., Barlage, M. J., Yu, W., and Duda, M. G. : The
684 Weather Research and Forecasting Model: Overview, System Efforts, and Future Directions, *Bulletin of the American
685 Meteorological Society*, 98(8), 1717-1737, 2017.

686 Rasmussen, E. N., J. M. Straka, R. P. Davies-Jones, C. A. Doswell, F. H. Carr, M. D. Eilts and D. R. MacGorman:
687 Verification of the Origins of Rotation in Tornadoes Experiment: VORTEX. *Bull. Amer. Meteor. Soc.*, 75, 995–1006,
688 1994.

689 Ryzhkov, A., Pinsky, M., Pokrovsky, A., and Khain, A.: Polarimetric Radar Observation Operator for a Cloud Model
690 with Spectral Microphysics. *J. Appl. Meteor. Climatol.*, 50, 873–894, 2011.

691 Shusse, Y., and Tsuboki, K.: Dimension Characteristics and Precipitation Efficiency of Cumulonimbus Clouds in the
692 Region Far South from the Mei-Yu Front over the Eastern Asian Continent, *Monthly Weather Review*, 134(7), 1942-
693 1953.,

694 Stein, T. H. M., Hogan, R. J., Clark, P. A., Halliwell, C. E., Hanley, K. E., Lean, H. W., Nicol, J. C., and Plant, R. S.: The
695 DYMECS Project: A Statistical Approach for the Evaluation of Convective Storms in High-Resolution NWP Models,
696 *Bulletin of the American Meteorological Society*, 96(6), 939-951, 2015.

697 Steiner, M., Houze, R. A., Jr., and Yuter, S. E. : Climatological Characterization of Three-Dimensional Storm Structure
698 from Operational Radar and Rain Gauge Data, *Journal of Applied Meteorology and Climatology*, 34(9), 1978-2007,
699 1995.

700 Wurman, J., Dowell, D., Richardson, Y., Markowski, P., Rasmussen, E., Burgess, D., Wicker, L., & Bluestein, H. B. :
701 The Second Verification of the Origins of Rotation in Tornadoes Experiment: VORTEX2, *Bulletin of the American
702 Meteorological Society*, 93(8), 1147-1170, 2012.

703 van den Heever, S. C., Grant, L. D., Freeman, S. W., Marinescu, P. J., Barnum, J., Bukowski, J., Casas, E., Drager, A. J.,
704 Fuchs, B., Herman, G. R., Hitchcock, S. M., Kennedy, P. C., Nielsen, E. R., Park, J. M., Rasmussen, K., Razin, M. N.,
705 Riesenber, R., Dellaripa, E. R., Slocum, C. J., Toms, B. A., & van den Heever, A. : The Colorado State University

706 Convective Cloud Outflows and UpDrafts Experiment (C3LOUD-Ex), Bulletin of the American Meteorological
707 Society, 102(7), E1283-E1305.

708 Wurman, J.: The DOW mobile multiple-Doppler network. Preprints, 30th Int. Conf. on Radar Meteorology, Munich,
709 Germany, Am. Meteorol. Soc., 95–97, 2001.

710 Wurman, J., D. Dowell, Y. Richardson, P. Markowski, E. Rasmussen, D. Burgess, L. Wicker, H.B. Bluestein: The Second
711 Verification of the Origins of Rotation in Tornadoes Experiment: VORTEX2. Bull. Amer. Meteor. Soc., 93, 1147-
712 1170, doi: 10.1175/BAMS-D-11-00010.1, 2012.

713 Zängl, G., Reinert, D., Rípodas, P. and Baldauf, M. : The ICON (ICOsahedral Non-hydrostatic) modelling framework of
714 DWD and MPI-M: Description of the non-hydrostatic dynamical core. Q.J.R. Meteorol. Soc., 141: 563-579.
715 <https://doi.org/10.1002/qj.2378>, 2015.

716
717
718
719 Table 1. Radar scan strategies simulated in this study.

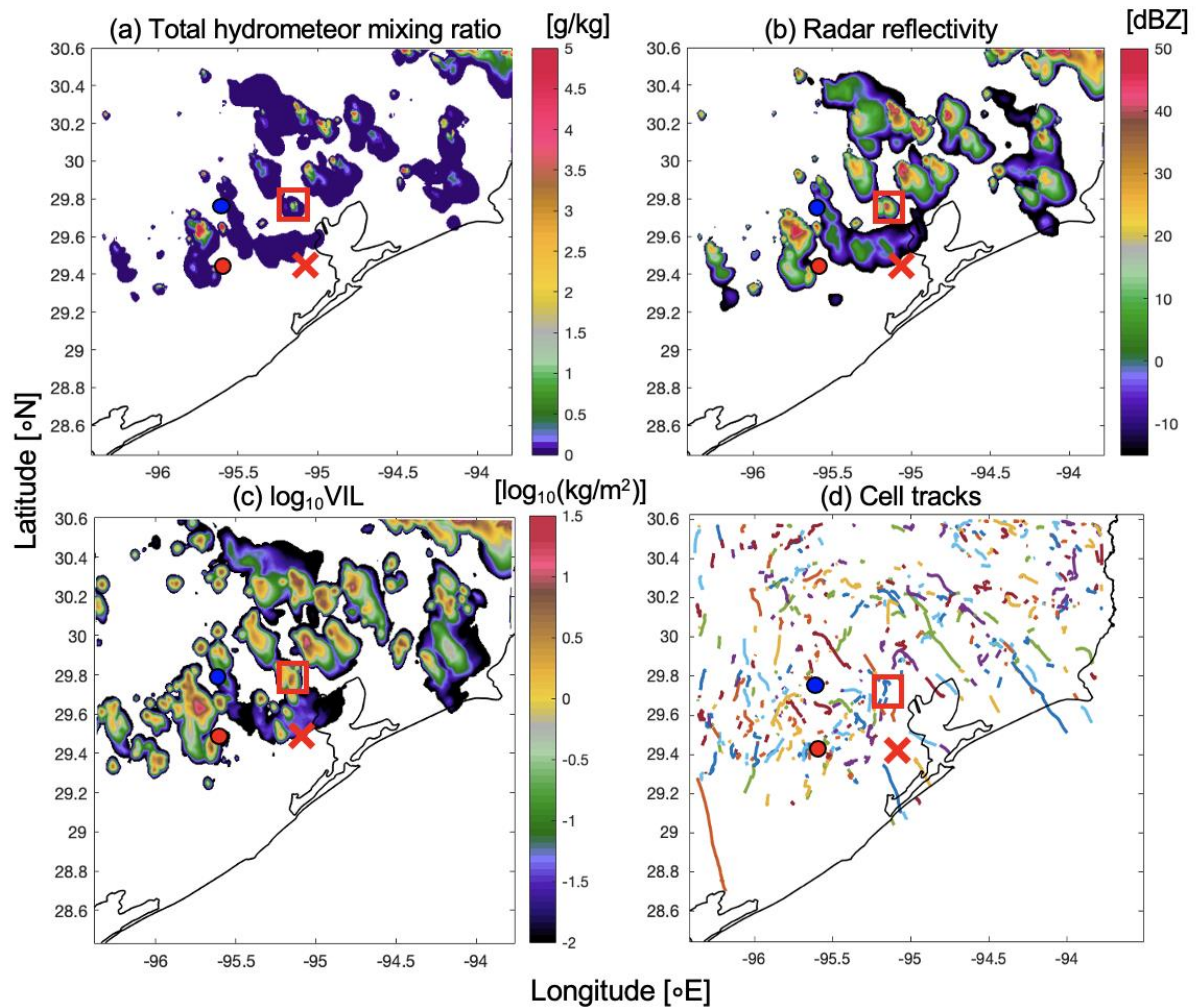
Strategy	Full elevation scan for an azimuth sector tracking cells (1-min RHI, 2-min SEC)	5-min volume coverage pattern (5-min VCP)	Full elevation/azimuth scan (Full)
Beam width	1.0°	0.9°	1.0°
Elevation angles	From 0.5° to 89.5° every 1°	0.48, 0.88, 1.32, 1.8, 2.42, 3.12, 4.0, 5.1, 6.42, 8.0, 10.02, 12.48, 15.6, and 19.51°	From 0° to 90° every 1°
Azimuth range	14.5° at 40 km radar range (Sector to cover a 10-km width centered around the individual cells with 1° spacing)	From 0° to 360° with a 0.5° increment	From 0° to 360° with a 1.0° increment
Time for volume scan	1 minute or 2 minutes*	5 minutes	1 minute

720 *With the radar beam width of 1°, the total number of beams for the sector scan is 90 (over elevation) x 14 (over azimuth)
721 = 1260 beams. Assuming that each beam needs ~96 radar samples, the total number of pulses is 120960. This takes 1-2
722 min with typical pulse repetition ratios (1.5 - 2.5 kHz) for C- and X-band radars. See detailed discussion in Sect. 2.4.2
723

724 Table 2. The root-mean-square error (RMSE) of the retrieved updraft averaged over the regions with reflectivity ≥ 40 dBZ
 725 at four different altitudes as well as all heights for a variety of scan strategies for the entire lifetime.

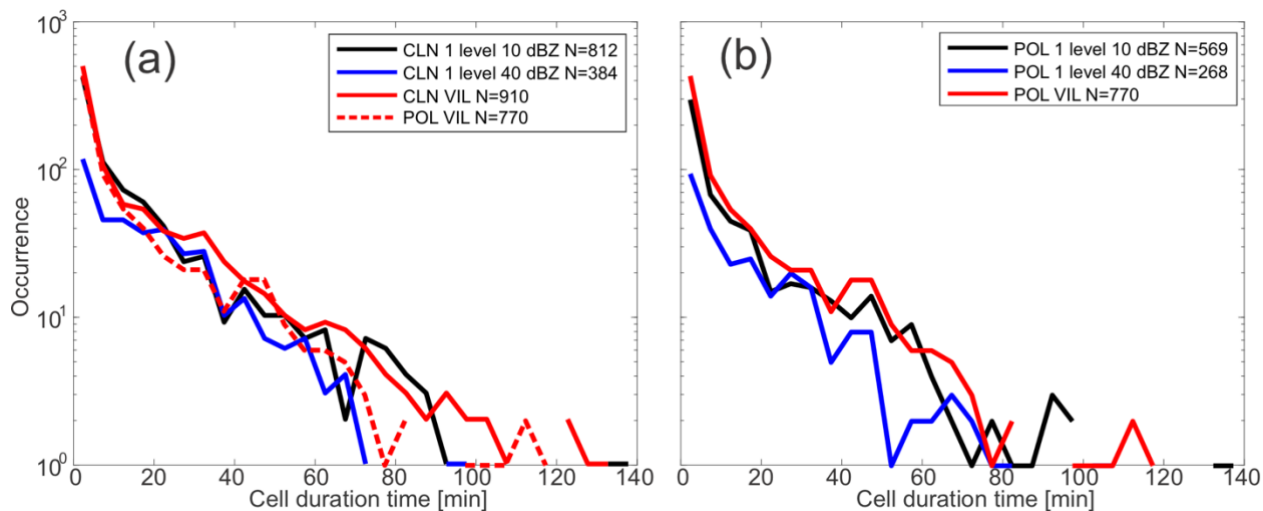
	1. Two 1-min RHIs (2RHIs)	2. Two 5-min VCPs (2VCPs)	3. One 1-min RHI + one 5-min VCP (RHIVCP)	4. Two 1-min RHIs + one 5-min VCP (2RHIVCP)
10 km	4.794	16.82	7.995	4.800
8 km	5.371	7.396	5.609	5.112
6 km	5.862	6.601	4.764	4.895
4 km	4.232	3.178	3.625	3.511
All heights	5.030	6.763	5.539	4.535

726



727

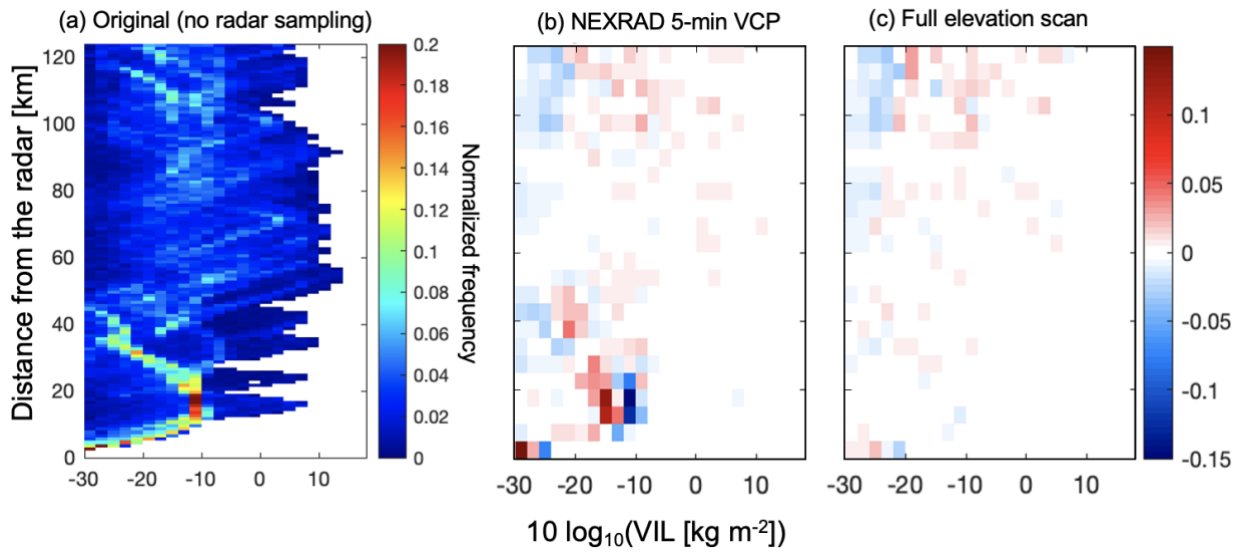
728 Fig. 1: (a) A snapshot of the RAMS-simulated total hydrometeor condensate field at 21:09 UTC at 5.5 km ASL; (b) CR-SIM
 729 simulated radar reflectivity field at the same height and same time as (a); (c) vertically integrated liquid (VIL) estimated from
 730 the CR-SIM C-band total reflectivity (from total liquid and ice hydrometeor condensate) at the same time as (a); and (d) tracks
 731 of precipitating convective cells detected between 20:00 and 23:59 UTC using *tobac*. On each panel, the red “X” marks the location
 732 of a radar performing 5-min VCP (i.e., NEXRAD KHGX), the red solid dot represents the location of a radar performing a
 733 different 5-min VCP or RHI, and the blue solid dot represents the location of another radar performing RHI. The red rectangle
 734 represents the tracked cell of interest used for multi-Doppler radar retrieval and polarimetric evolution analysis.



735

736 Fig. 2: Frequency distributions of cell duration time from the *tobac* cell tracking using VIL (red), 10 dBZ threshold at 2 km
 737 height (blue), and 40 dBZ threshold at 2 km height (black) for (a) CLN and (b) POL cases. The legend displays the total
 738 number of detected cells (N) for each tracking parameter utilized. Panel (a) also includes the cell tracking using VIL for the
 739 POL case shown as the red dashed line. The time bin size for the frequency distribution plots is 5 min.

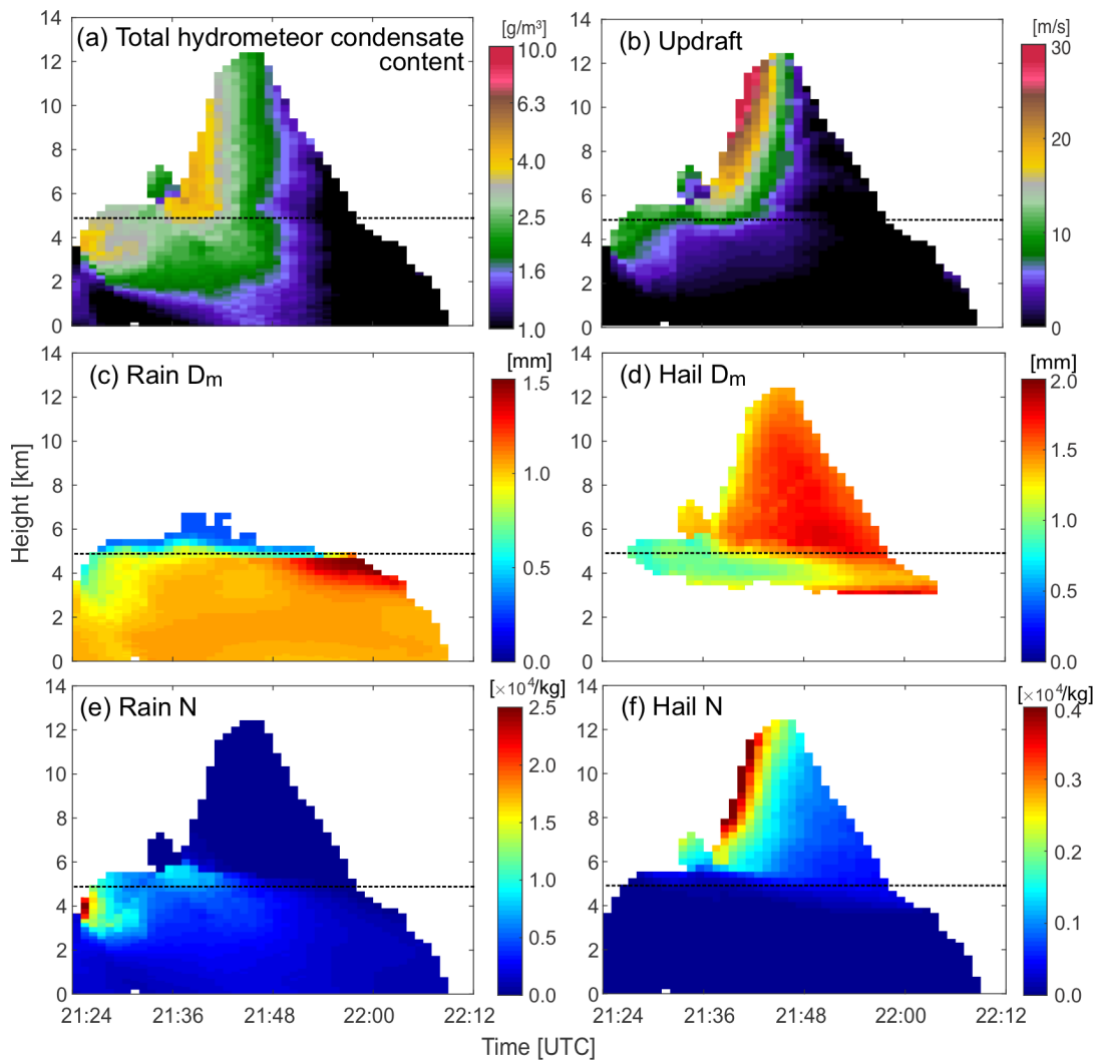
740



741

742 **Figure 3: (a) Contoured frequency by distance (from the radar) distribution of the VIL from the original, cartesian model grid**
 743 **from the 1-minute output over the 4-hour analysis period; (b) difference between the VIL from the 5-min VCP scan strategy and**
 744 **(a); and (c) difference between the VIL from the Full scan strategy and (a). The VILs from the 5-min VCP and Full scan strategies**
 745 **are estimated from the gridded reflectivity fields with 250 m horizontal and vertical spacing and 1-minute output over the 4-hour**
 746 **period.**

747



748

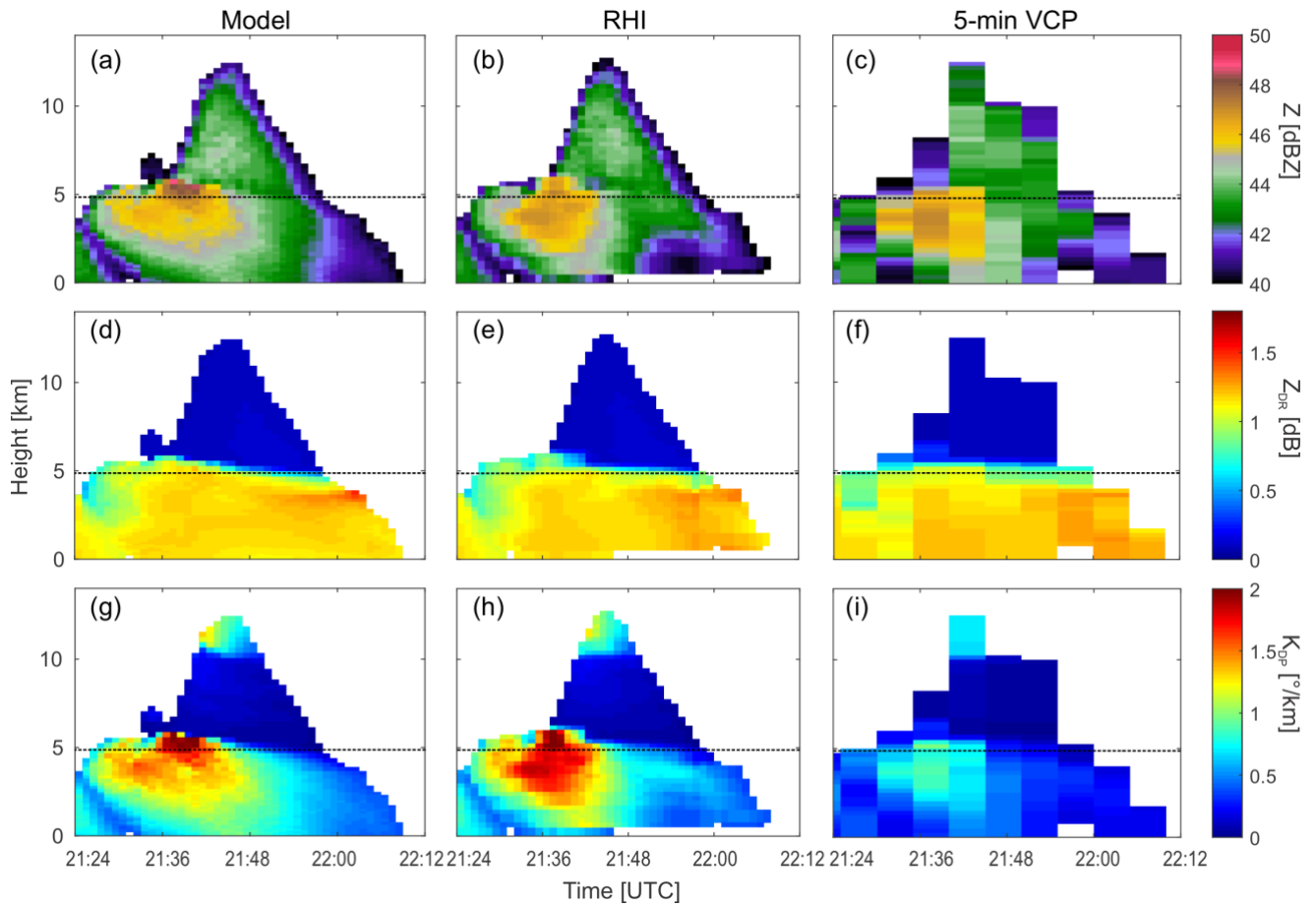
749

750

751

752

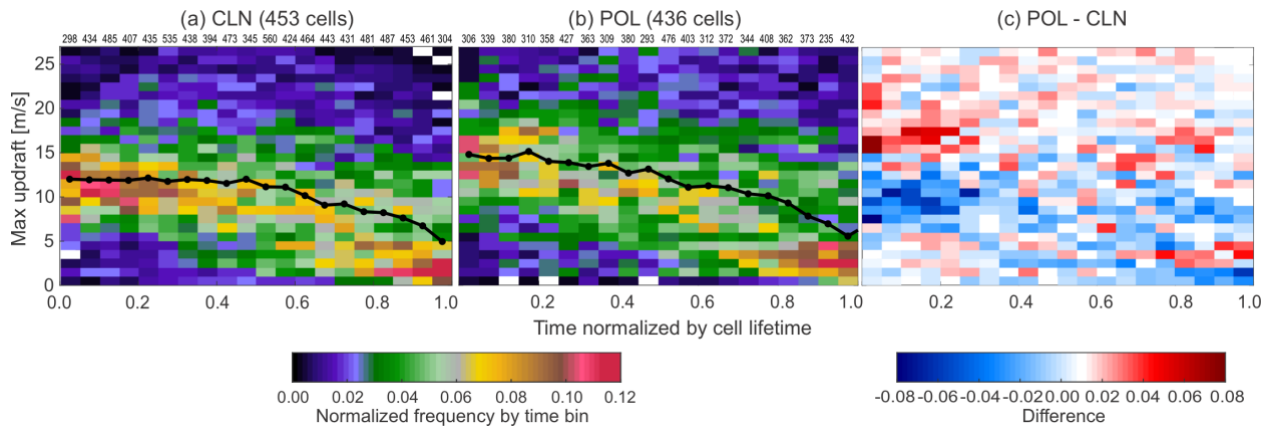
Fig. 4: Height-versus-time cross sections of the (a) total hydrometeor condensate content, (b) updraft, (c-d) the mass-weighted mean diameter (D_m) for (c) rain and (d) hail, and the number density (N) for (e) rain and (f) hail, averaged for areas with reflectivity > 40 dBZ of the selected convective cell from the CLN case. Dashed line in each panel represents a 0°C isotherm of domain-averaged temperature.



753

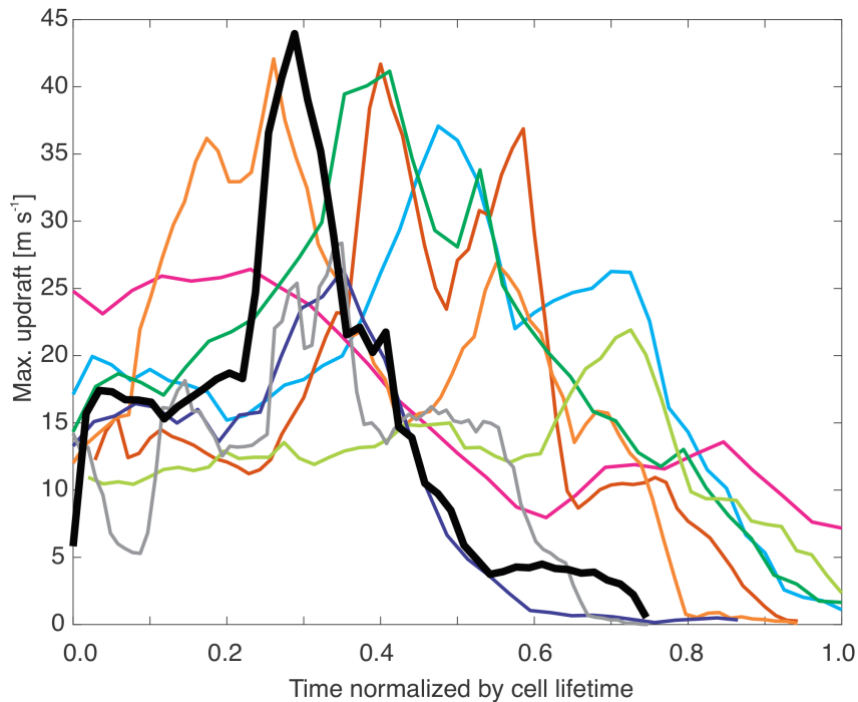
754 **Fig. 5: Time-height cross sections of C-band radar reflectivity (top row), Z_{DR} (middle row), and K_{DP} (bottom row), averaged for**
 755 **areas with reflectivity > 40 dBZ for the selected convective cell for (a,d,g) the model simulation truth, (b,e,h) simulated RHI**
 756 **tracking strategy, and (c,f,i) simulated 5-min volume scan strategy. The cell in this figure is the same as that shown in the box in**
 757 **Fig. 4 and is from the CLN case. Note that the NEXRAD S-band frequency is assumed for the 5-min VCP simulation, while C-**
 758 **band frequency is assumed for the model and RHI simulation. Therefore, the K_{DP} values in this figure include the frequency**
 759 **dependency. Dashed line in each panel represents a 0°C isotherm of domain-averaged temperature.**

760



761

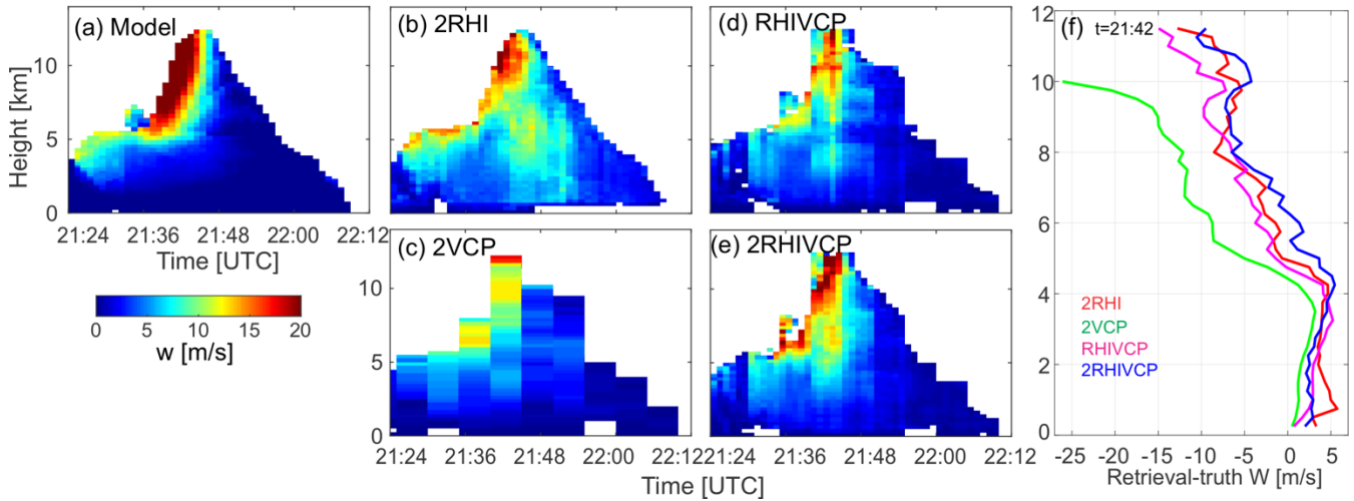
762 **Fig. 6:** Frequency of maximum updraft magnitudes in detected individual cells as a function of time normalized by the cell
 763 duration for the (a) CLN and (b) POL case simulations, and (c) the difference between the CLN and POL cases (POL – CLN).
 764 Here we present only those deep convective cells with 20 dBZ echo top heights that exceeded the freezing level during their
 765 lifetimes. Color shading in (a) and (b) represents normalized frequency by cell lifetime, and that in (c) represents the difference
 766 in the normalized frequency. The sample size at each time bin is presented on the top of (a) and (b). Black lines in (a) and (b)
 767 represent the median value in each time bin.



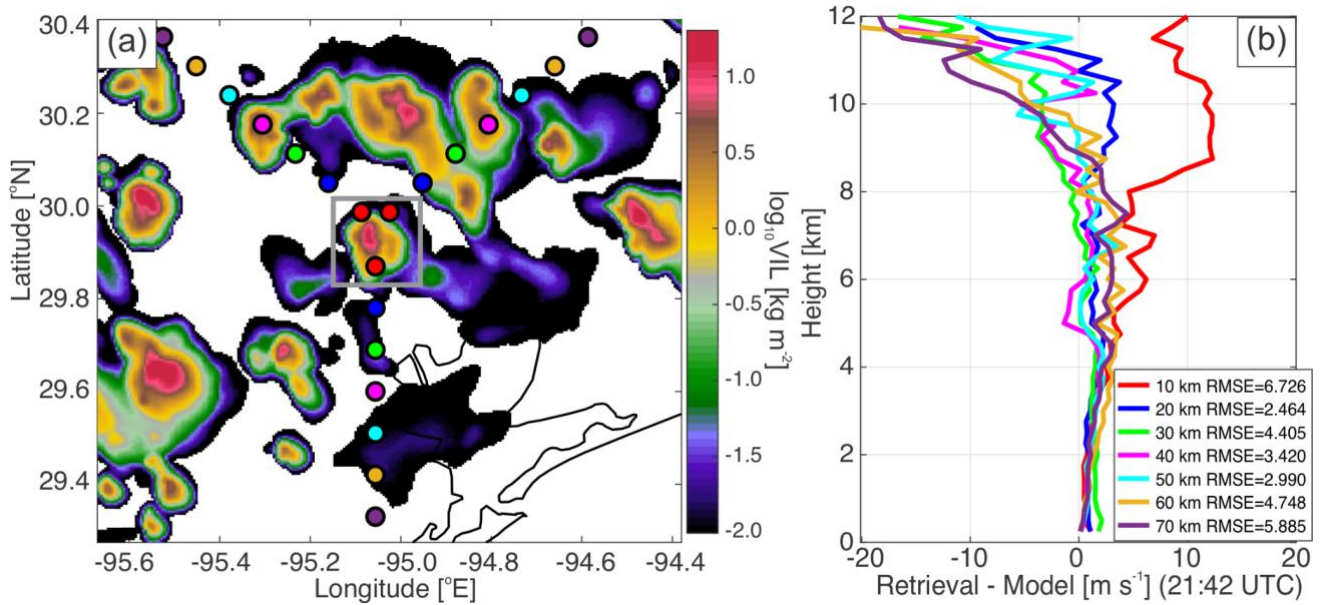
768

769 **Figure 7:** Maximum updraft velocity in the cell column at each time represented as a function of the normalized lifetime for the
 770 nine deep convective cells from the CLN simulation. These cells were randomly selected, as described in Section 3.2, and were
 771 required to have the maximum radar reflectivity greater than 45 dBZ, the echo top height of 40 dBZ exceeding 5 km in altitude,

772 and the echo top height of 20 dBZ extending above 8 km altitude during the storm lifecycle. The black line represents the target
 773 cell that was analyzed for the present OSSE. Note that because the plot displays the maximum updraft found in regions with
 774 reflectivity greater than 45 dBZ, some lines do not end at time=1.0 when the maximum reflectivity is below 45 dBZ.
 775

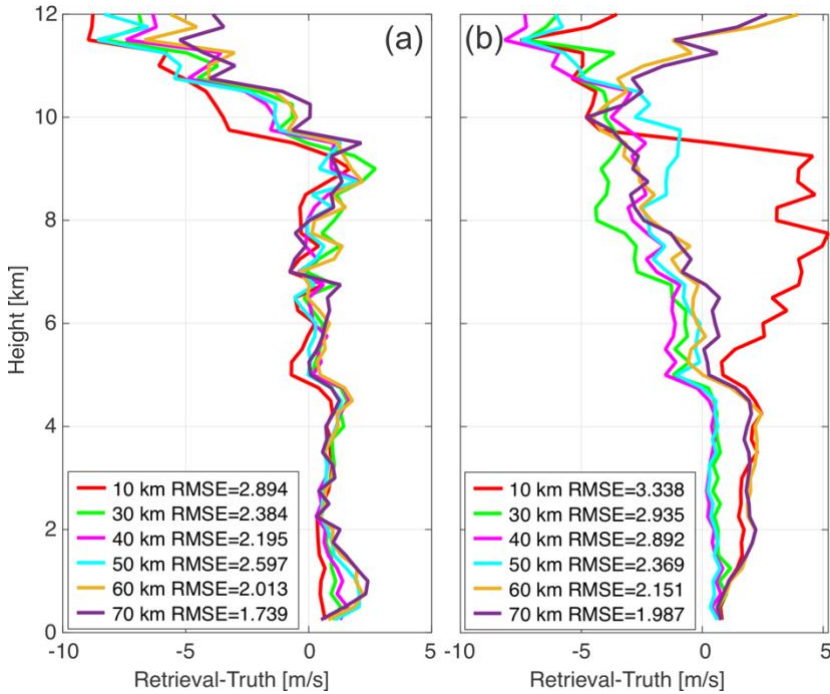


776
 777 **Fig. 8: Height-time cross sections of the updraft velocity averaged over the area with reflectivity > 40 dBZ from (a) the model**
 778 **(truth) and (b-e) the simulated retrievals, as well as the (f) errors of the simulated multi-Doppler vertical velocity retrievals**
 779 **(retrieval - truth) at 21:42 UTC, when the maximum updraft was produced by the cell.**

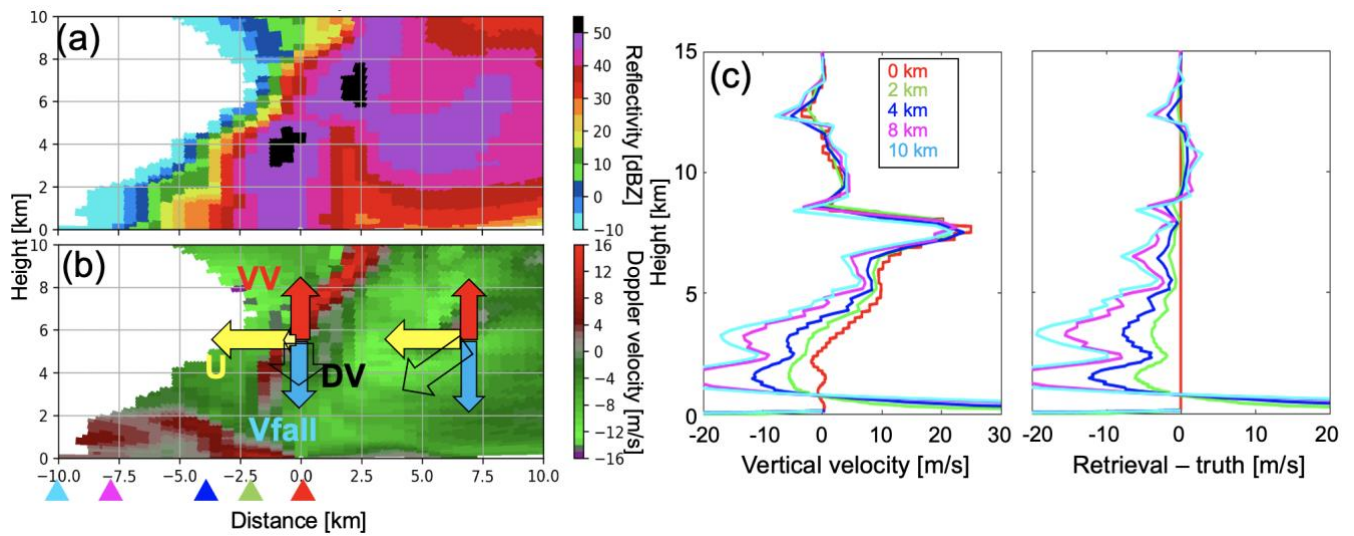


780
 781

782 **Fig. 9:** (a) Horizontal distribution of VIL centered around one identified convective cell (gray box, the same cell shown in Figs.
 783 4, 5, and 8) at 21:42 UTC from the CLN simulation and (b) vertical profiles of errors of simulated retrievals (retrieval - model)
 784 averaged over a region with reflectivity > 30 dBZ at 21:42 UTC for the identified convective cell. The colored dots in (a) represent
 785 the radar locations for the multi-Doppler radar wind retrievals. The colors of the dots correspond to the colors of the set of the
 786 radars for the multi-Doppler radar wind retrievals shown in (b). The two radars to the north of the cell performed 2-min RHIs,
 787 and the other performed 5-min VCP. The RMSE for each profile is displayed in (b).
 788



789 **Fig. 10:** Vertical profiles of errors of simulated retrievals (retrieval - model) averaged over a region with reflectivity > 30 dBZ
 790 at 21:42 UTC for the identified convective cell using the three radars where the two are fixed at distance = 20 km (blue dots in
 791 Fig. 9a) while one is moved (dots with the other colors in Fig. 9a). In (a) the 2-min SEC radar (at the northwest corner of the
 792 triangle in Fig. 9a) is moved, and in (b) the 5-min VCP radar (at the south corner of the triangle in Fig. 9a) is moved. The colors of
 793 lines correspond to the dot's colors for the moved radar.
 794
 795



796

797

798

799

800

801

802

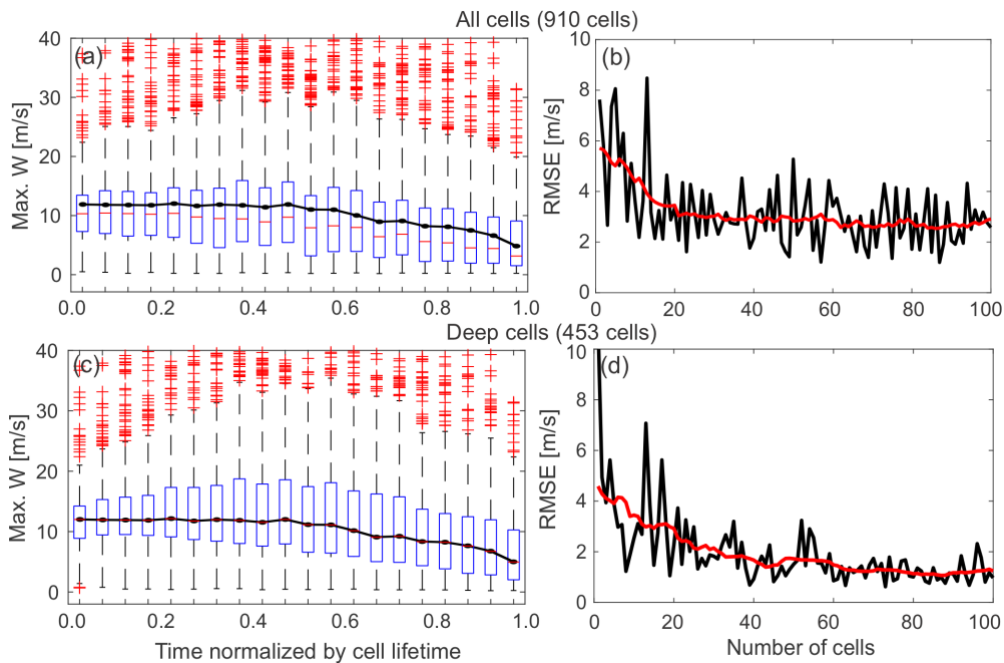
803

804

805

806

Fig. 11: Vertical cross section of (a) radar reflectivity and (b) Doppler velocity from the simulated RHI measurement for a convective cell and vertical profiles of (c) retrieved vertical air motion and (d) errors (retrieval – model), simulated with different distances between the radar and the center of the convective cell (distance = 0 km in b) at 21:42 UTC. The location of the radars from the center of the convective cell in (c-d) are indicated by their corresponding colored triangle in panel (b). A negative Doppler velocity in (b) represents motion toward the radar. In Panel (b), arrows represent examples of the Doppler velocity vector and the components at two range-height bins ($[x,y]=[0 \text{ km}, 5 \text{ km}]$ and $[7.5 \text{ km}, 5 \text{ km}]$); the clear arrows with black line represent the observed Doppler velocity (labeled as DV), the red arrows represent vertical velocity component (labeled as VV), the yellow arrows represent horizontal wind component along the vertical cross section (labeled as U), and the light blue arrows represent the component of the particle fall velocity (labeled as Vfall). These examples assume that each component at the two points has the same value, but the scale does not represent a specific value.



807

808

809

810

811

812

813

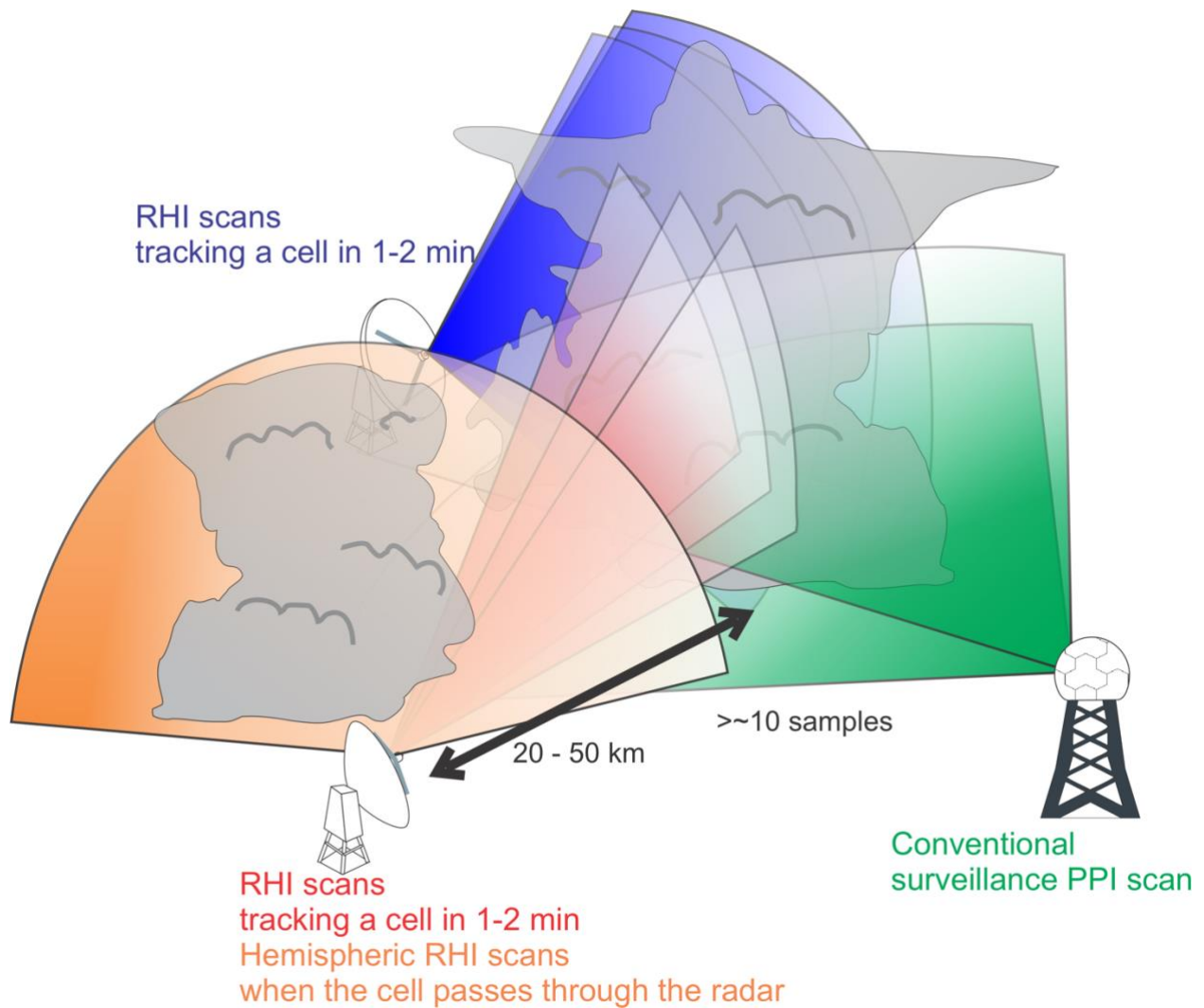
814

815

816

817

Figure 12: (a,c) Boxplots of maximum vertical velocity as a function of the normalized lifetime from all convective cells detected (910 cells including deep and shallow cells) from the CLN case and from the deep convective cells (453 cells) defined in Fig. 6a, respectively. For each boxplot, the central red mark indicates the median, and the bottom and top edges of the box indicate the 25th and 75th percentiles, respectively. The whiskers extend to the most extreme data points excluding outliers. Outliers are plotted individually using the cross symbol. Black solid lines in (a) and (c) represent the temporal evolution of the median values of maximum updrafts for deep cells as a function of time. (b,d) The RMSEs of median values of the maximum vertical velocity as a function of the number of cells randomly sampled from all convective cells detected in the CLN simulation (b) and from deep convective cells defined in Fig. 6a (d). The RMSEs are estimated from the median profiles as a function of the normalized lifetime from the random sampling and that from all deep convective cells (black line in Fig. 6a).



818

819 **Figure 13: A schematic image of a suggested scan strategy optimized for observing convective cell evolution. Optimal cell tracking**
 820 **is achieved by frequent RHI scans from more than one radar (blue and red scans) in addition to the operational PPI volume scans**
 821 **generally performed by the NEXRAD radars (green scans). The schematic also suggests an optimal hybrid radar scan strategy**
 822 **which switches between cell tracking by frequent RHI measurements and hemispheric RHI measurements depending on the**
 823 **distance between the radar and the target cell (red and orange scans).**

824

825